PCCP

Physical Chemistry Chemical Physics

rsc.li/pccp

25 YEARS
ANNIVERSARY

ROYAL SOCIETY
OF **CHEMISTRY**
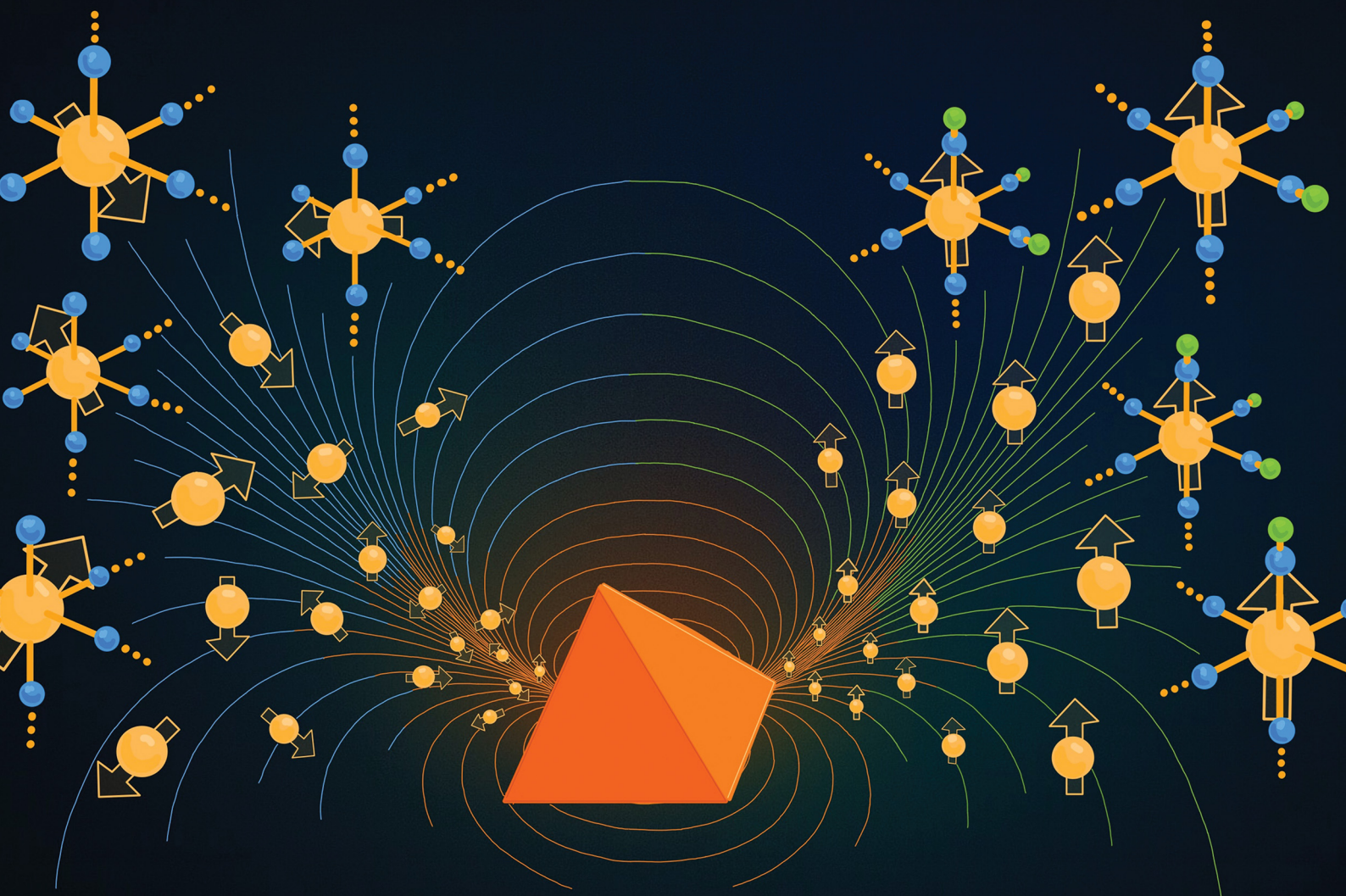
PAPER
Jana Pavlů *et al.*
First-principles insights into structure and magnetism in
ultra-small tetrahedral iron oxide nanoparticles

PCCP
Owner Societies

Check for updates

First-principles insights into structure and magnetism in ultra-small tetrahedral iron oxide nanoparticles

Valentína Berecová, [ID] ab Martin Friák, [ID] a Naděžda Pizúrová [ID] a and Jana Pavlů [ID] *b

Structural and magnetic properties of ultra-small tetrahedron-shaped iron oxide nanoparticles were investigated using density functional theory. Tetrahedral and truncated tetrahedral models were considered in both non-functionalized form and with surfaces passivated by pseudo-hydrogen atoms. The focus on these two morphologies reflects their experimental relevance at this size scale and the feasibility of performing fully relaxed, atomistically resolved first-principles simulations. Moreover, a novel application of pseudo-hydrogen passivation to magnetic iron oxide nanoparticles is introduced as a practical strategy to probe intrinsic surface effects on magnetism while reducing artefacts from dangling bonds. Although these terminations are simplified representations, they were found to capture essential aspects affecting nanoparticle behavior. In non-functionalized models, significant distortions due to the undercoordination were observed, including Fe−O bond shortening by up to 0.46 Å and enhanced magnetic moments on oxygen atoms. These changes disrupted ferrimagnetic ordering, with spin-flipping in both tetrahedral and octahedral sublattices leading to an almost 90% reduction in total magnetization. Upon passivation, these effects were largely mitigated: Fe−O bond lengths became more uniform and ferrimagnetic alignment was stabilized as the energetically preferred state. Averaged spin−flip energies were computed to be 58 meV and 72 meV for both geometries, which is markedly lower than values for bulk γ-Fe$_2$O$_3$ (407−534 meV), suggesting that magnetic disorder may emerge during synthesis at typical growth temperatures. Charge transfer analysis further showed that surface coordination strongly affects electron distribution, with surface capping restoring near bulk-like charge states.

Introduction

Iron oxide nanoparticles (IONPs), especially structurally related to magnetite (Fe$_3$O$_4$) and maghemite (γ-Fe$_2$O$_3$), have attracted significant attention due to their remarkable magnetic properties like superparamagnetism,[1] magnetoresistance,[2,3] high saturation magnetization[4–6] and low coercivity.[1] Owing to their combined structural and physical properties, they are used in various applications, including environmental protection,[7–10] spintronics,[3] data storage and sensor technologies.[11]

Thanks to the ability to synthesize biocompatible IONPs with low cytotoxicity,[12,13] they can be utilized in different biomedical fields, such as magnetic separation,[14] carriers for drug delivery,[15–17] contrast agents for magnetic resonance imaging (MRI)[18–21] and heating agents in local magnetic hyperthermia treatment.[22–26] For many biological applications, the size of the nanoparticles plays a crucial role in determining their effectiveness. Multiple studies have shown that monodisperse nanoparticles with cores smaller than 20 nm[27–31] often yield better results. These small iron oxide nanoparticles, commonly referred to as superparamagnetic iron oxide nanoparticles (SPIONs),[27,28] exhibit prolonged circulation times[29] and can navigate biological barriers and tissues more efficiently, making them particularly advantageous for medical use. Some researchers have further refined this classification by defining ultra-small superparamagnetic iron oxide nanoparticles (USPIONs),[30] typically with core sizes below 5 nm. For instance, Wei *et al.* synthesized USPIONs with an estimated diameter of 1.3 nm and demonstrated their ability to enhance longitudinal relaxation (T_1), thereby brightening the signal in T_1-weighted MRI,[32] due to a magnetically disordered surface layer. Their analysis also revealed that these nanoparticles exhibit a structure similar to maghemite and magnetite.

Recent studies have shown that IONPs with an anisotropic shape, such as cubes,[33–35] polyhedrons,[33,36] nanorods[37] and

[a] *Institute of Physics of Materials, v. v. i., Czech Academy of Sciences, Žižkova 22, Brno, 616 00, Czech Republic*

[b] *Masaryk University, Faculty of Science, Department of Chemistry, Kotlářská 2, Brno, 611 37, Czech Republic. E-mail: houserova@chemi.muni.cz*

stars,[33] often outperform their spherical counterparts in various biomedical applications. For example, Zhou et al.[38] successfully synthesized tetrahedral and truncated polyhedral iron oxide nanoparticles and found that their T_1 and T_2 relaxation times were significantly shortened compared to the spherical NPs. This enhancement was attributed to their exposed facets and anisotropic magnetic properties, making them highly effective MRI contrast agents.

While the practical applications of magnetic iron oxide nanoparticles are well studied and established, a fundamental understanding of how microscopic parameters – such as size, shape, composition, and surface effects – influence their magnetic properties remains an area of ongoing research.

Computational studies employing density functional theory (DFT) have primarily focused on the structural, geometric and magnetic properties of small neutral stoichiometric $(Fe_2O_3)_n$ clusters with values n ranging from 1–5[39–41] up to 10, see ref. 42. Magnetic states of additional $(FeO)_m$ ($m \leq 16$)[43,44] and Fe_nO_m ($n = 1–5$)[45] cluster systems were analyzed in previous publications as well. Gutsev et al.[46] also investigated how functionalization affects the properties of $(Fe_2O_3)_4$ clusters, showing that adding up to 18 hydrogen atoms alters both their structure and spin magnetic moments. Several authors have explored the possible adsorption behavior of the D-penicillamine[47] molecule, Melphalan[48] and Flutamide[49] drugs on the surface of $Fe_6(OH)_{18}(H_2O)_6$ ring clusters. In addition, larger clusters[50] with compositions $Fe_{25}O_{30}$ and $Fe_{33}O_{32}$ were studied using spin-polarized generalized gradient approximation (SGGA) methods, both with and without the Hubbard +U correction (SGGA + U), revealing the energetic preference for ferrimagnetic ordering. López et al.[51] analyzed the ferrimagnetic configuration of an even larger spherical nanometre-sized $Fe_{45}O_{68}$ cluster and investigated the possibility of spin-flipping in the tetrahedral sublattice of the $Fe_{17}O_{16}$ cluster, which they referred to as a partial ferrimagnetic state. Beyond studying the electronic structure of iron oxide clusters at the quantum mechanical level, several theoretical studies have included simulations of small nanoparticle models (up to 5 nm), employing molecular dynamics simulations[52,53] to explore their geometric structure and crystallization processes.

The aim of this study is to investigate structural, magnetic and thermodynamic properties of USPIONs with atomistic precision by using density functional theory. Our analysis captures the effects of surface atoms, local coordination environments and spin configurations. We deliberately focus on an in-depth analysis of tetrahedral nanoparticle models, particularly since this morphology was successfully obtained at the size scale studied here (Fig. 1). Notably, the authors of ref. 52, using molecular dynamics simulations, also reported that the tetrahedral morphology remains stable at sizes up to 3 nm, further supporting the relevance of our chosen morphology. To further assess the influence of surface effects, additional calculations incorporating pseudo-hydrogen atoms were performed to approximate the impact of surface functionalization. To our knowledge, pseudo-hydrogen atoms have not yet been employed to model surface capping on iron oxide
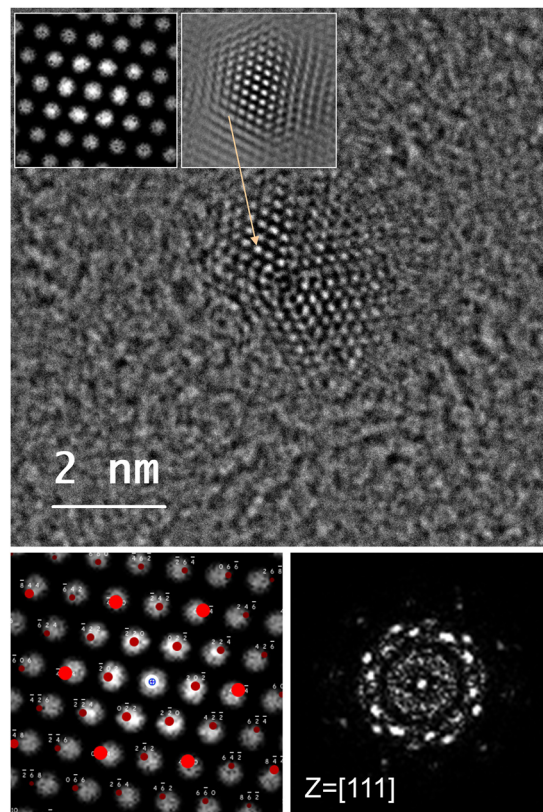

Fig. 1 Transmission electron microscopy (TEM) image of ultra-small anisotropic tetrahedron-shaped iron oxide nanoparticles, that we synthesized, highlighting exposed {111} crystal facets, combined with the corresponding Fourier transform.

nanoparticles. This approach has been mainly applied to slab models to eliminate artificial electric fields[54,55] or to semiconductor NPs such as CdSe, TiO$_2$ and GaAs to improve electronic structure predictions.[56,57] However, its impact on magnetic properties remains unexplored, representing a gap in the computationally accessible modelling of magnetic nanomaterials. The resulting systems were compared with the behavior of bulk magnetite (Fe_3O_4) and maghemite (γ-Fe_2O_3).

Computational details

The *ab initio* results presented in this study were calculated using density functional theory[58,59] as implemented in the Vienna *ab initio* simulation package (VASP).[60–63] The GGA method with PBE parametrization[64,65] was used to describe the contribution of exchange and correlation effects. Projector augmented wave (PAW)[66,67] potentials were used with the following atomic orbitals treated as valence states: the 3d, 4s orbitals and semicore 3p orbitals for Fe; and the 2s and 2p orbitals for O. For pseudo-hydrogen atoms used to saturate dangling bonds on the surfaces of the nanoparticles, both fractional valence states ($Z = 0.5$ and $Z = 1.5$) and the standard valence states ($Z = 1$) were applied. The plane wave cut-off energy was set to 500 eV for all systems. For the integration over
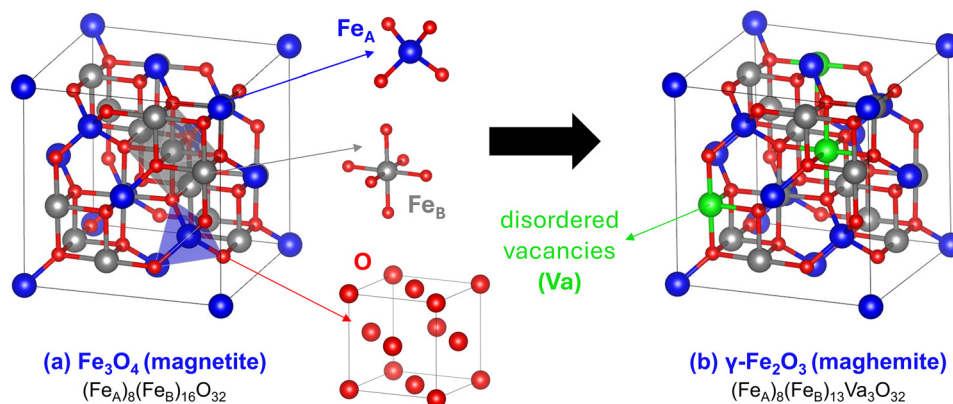
This journal is © the Owner Societies 2025

Phys. Chem. Chem. Phys., 2025, **27**, 21424–21440 | **21425**

Fig. 2 Inverse spinel structure of (a) magnetite (Fe_3O_4) and (b) vacancies containing maghemite (γ-Fe_2O_3). Red spheres denote the O atoms in face-centered cubic (fcc) lattice. Blue and grey spheres correspond to the tetrahedral (Fe_A) and octahedral (Fe_B) iron atoms, respectively. Green spheres correspond to vacancies Va.

the Brillouin zone, different smearing methods were selected based on the structure: (a) the tetrahedron method with Blöchl correction[68] for γ-Fe_2O_3 bulk, (b) the Methfessel–Paxton scheme[69] for Fe_3O_4 bulk and iron oxide nanoparticles and (c) the Gaussian smearing[70] for the nanoparticles coated with pseudo-hydrogen atoms. The smearing width was set to 0.1 eV for methods (b) and (c). The Brillouin zone was sampled using a $6 \times 6 \times 6$ Monkhorst–Pack k-mesh for bulk structures and a $2 \times 2 \times 2$ Monkhorst–Pack k-mesh for all nanoparticle models. Atomic forces were reduced below 0.02 eV Å^{-1}.

The computational cells for magnetite and maghemite were constructed based on crystallographic data from experimental publications,[71,72] while the nanoparticle morphologies were inspired by our experimental research. The analysis of the product, that we synthesized, performed using a Titan Themis 60–300 cubed transmission electron microscope, confirmed the presence of ultra-small tetrahedron-shaped IONPs enclosed by low-index {111} crystal facets (Fig. 1). This is in good agreement with the results obtained by Narnaware *et al.*,[73] who also reported similar morphology that was easily explained due to the lower surface energy of {111} facets compared to {100} and {110} facets.

Magnetite crystallizes in a cubic inverse spinel structure containing 56 atoms per unit cell, as shown in Fig. 2(a). The composition can be further expressed as $(Fe^{3+})_A(Fe^{3+}Fe^{2+})_BO_{32}$. The A-site iron atoms (8 Fe_A per unit cell) are tetrahedrally coordinated by oxygen, forming a diamond-like lattice. The remaining iron atoms, consisting of Fe^{3+} and Fe^{2+} ions in the ratio 1:1,[74] occupy the octahedral B-sites (16 Fe_B per unit cell). By introducing three iron vacancies[75] into the octahedral (Fe_B) sublattice of magnetite, the unit cell of maghemite is obtained, resulting in a stoichiometric formula of $Fe_2O_{3.05}$. This transformation occurs in nanoparticles at temperatures as low as 50 °C[76] and is accompanied by the oxidation[77] of Fe^{2+} to Fe^{3+}. Cubic γ-Fe_2O_3 structure (Fig. 2(b)) emerges specifically when the distribution of created vacancies is disordered.

Two different tetrahedral morphologies of nanometre-sized IONPs were generated: (a) a tetrahedron-shaped nanoparticle

(NP_{tetra}) with four {111} facets, consisting of 161 atoms (5 Fe_A, 40 Fe_B and 116 O), as shown in Fig. 3(a); and (b) a nanoparticle in the shape of a truncated tetrahedron ($NP_{trunc-tetra}$) with eight {111} facets, composed of 145 atoms (5 Fe_A, 36 Fe_B and 104 O), as shown in Fig. 3(b). The $NP_{trunc-tetra}$ morphology was derived from NP_{tetra} by selective removal of FeO_3 segments from all four vertices. The surface layers of NP_{tetra} and $NP_{trunc-tetra}$ are made up of oxygen atoms (O_{facet} and O_{edge}) bonded to octahedral Fe_B atoms in the subsurface layer. Both nanoparticles were properly isolated within periodic boundary conditions applied by the VASP code, which was achieved by encapsulating them in cubic computational cells filled with vacuum, each with an edge length of 32 Å. Other nanoparticle sizes in the ultra-small region were not analyzed, as preserving the Fe_A:Fe_B:O stoichiometry and surface termination requires scaling of all three species simultaneously, leading to larger models with ~400 atoms that could not be fully relaxed due to the high computational cost. Further size reduction beyond the truncated morphology will yield smaller clusters with little or no tetrahedral symmetry.

Two additional models of both nanoparticles, denoted as NPH_{tetra} (Fig. 3(c)) and $NPH_{trunc-tetra}$ (Fig. 3(d)), were created by bonding surface oxygen atoms to pseudo-hydrogen atoms (psHs). Pseudo-hydrogen atoms are a computational construct that assigns effective charges to unsaturated surfaces. In nanostructures, surface atoms often possess dangling bonds (DBs) due to their reduced coordination compared to their bulk counterparts. The use of psH atoms helps to prevent artificial charge accumulation and provides a more realistic approach to the experimental conditions.[56,78] In simplified terms, pseudo-hydrogen atoms effectively mimic functionalization and surface capping without the explicit inclusion of ligands. However, they are unsuitable when chemical accuracy is required, such as in studies involving steric and electrostatic effects, binding energies, solvation or adsorption mechanisms. The assignment of effective charge values on psHs follows a simple chemical consideration known as the electron counting rule (ECR).[79] For instance, Suzdalev *et al.*[80] reported that magnetic nanoparticles
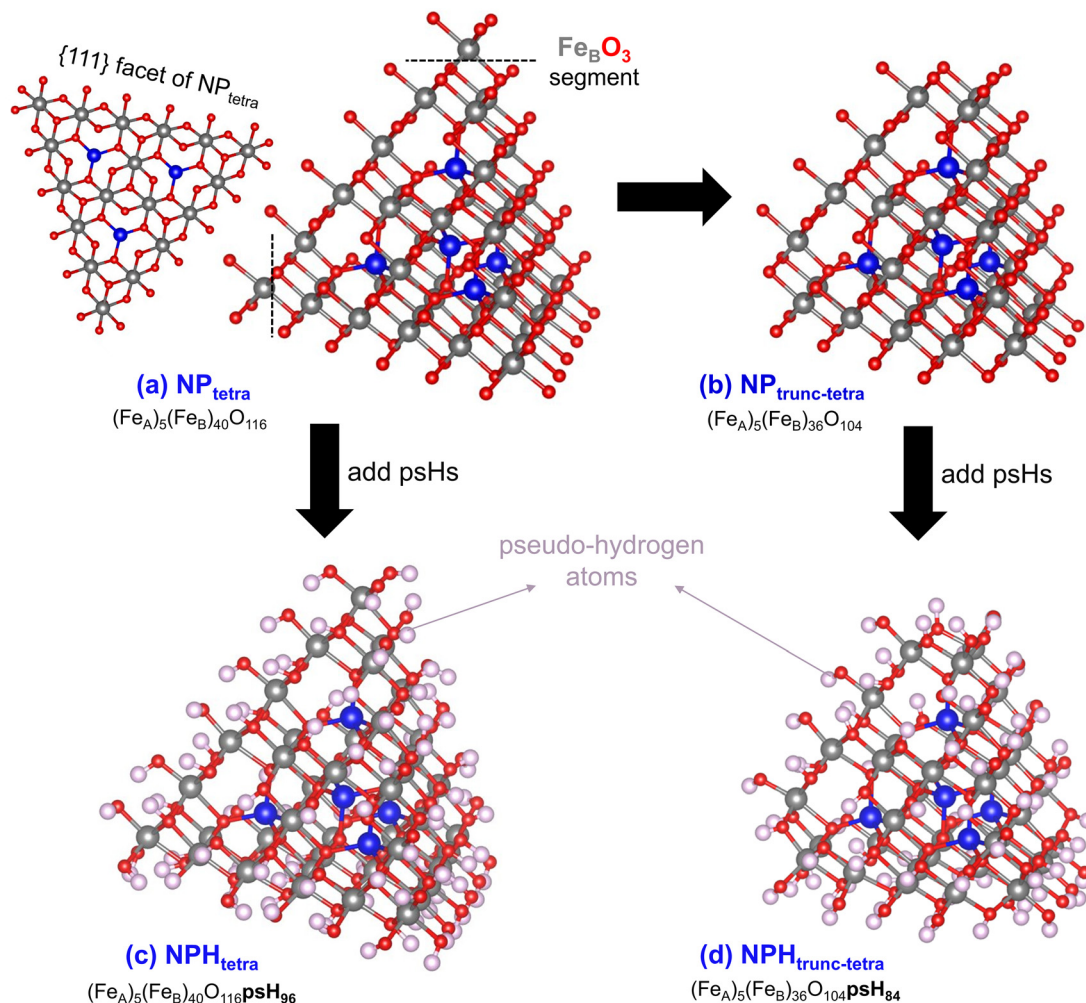
21426 | *Phys. Chem. Chem. Phys.*, 2025, **27**, 21424–21440

This journal is © the Owner Societies 2025

Fig. 3 The crystal structure of (a) NP_{tetra} including a view perpendicular to the {111} facet, (b) $NP_{trunc-tetra}$, (c) NPH_{tetra} and (d) $NPH_{trunc-tetra}$ shown without the $(32 \times 32 \times 32)$ Å^3 computational cell borders. The vertices removed from NP_{tetra} are indicated by the dashed lines in part (a). Red spheres represent oxygen atoms. Blue and grey spheres correspond to tetrahedral (Fe_A) and octahedral (Fe_B) iron atoms, respectively. Light pink spheres denote pseudo-hydrogen (psH) atoms.

assume an oxidized-like state including only Fe^{3+} species. In NP_{tetra} and $NP_{trunc-tetra}$ structures, these Fe^{3+} atoms located in the subsurface layer are coordinated by six oxygen atoms, while the inner oxygen atoms are bonded to four iron atoms. Assuming that each Fe_B atom donates 0.5 electrons per Fe_B–O bond, the DBs on surface oxygen atoms (Fig. 4(b)) are passivated with psHs assigned with different valencies:

1. $psH_{0.5} \rightarrow$ if one DB is present (Fig. 4(c)),
2. $psH_1 \rightarrow$ if two DBs are present (Fig. 4(d)),
3. $psH_{1.5} \rightarrow$ if three DBs are present (Fig. 4(e)).

The overall distribution of psHs with different charge states across NPH_{tetra} and $NPH_{trunc-tetra}$ is illustrated in Fig. 5. This approach ensures charge neutrality of the surface.

All systems in this study were calculated using a spin-polarized setting for collinear magnetism, with initial atomic magnetic moments set to ferrimagnetic ordering. For the γ-Fe_2O_3, NPH_{tetra} and $NPH_{trunc-tetra}$ structures, supplementary calculations with different magnetic configurations were also performed, followed by an energetics analysis. The heats of
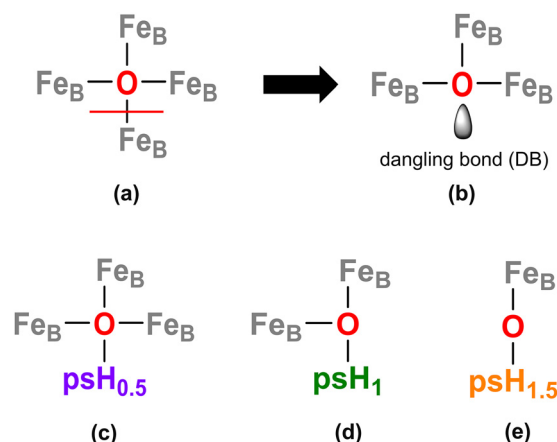

Fig. 4 Schematic representation of (a) oxygen atom in bulk-like coordination environment and (b) the formation of a dangling bond (DB) upon bond cleavage. Passivation of (c) one DB, (d) two DBs and (e) three DBs using pseudo-hydrogen atoms.
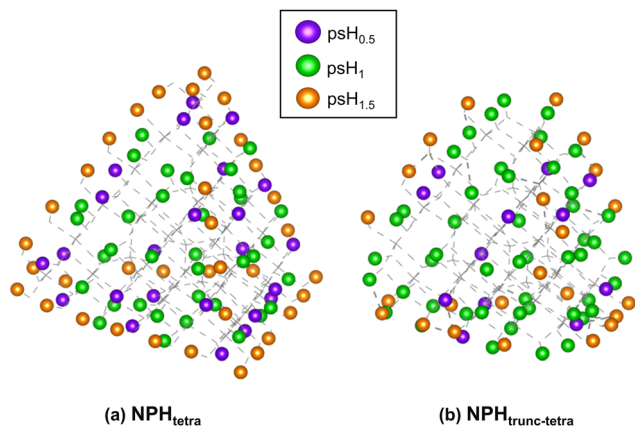
This journal is © the Owner Societies 2025

Phys. Chem. Chem. Phys., 2025, **27**, 21424–21440 | **21427**

Fig. 5 Distribution of pseudo-hydrogen atoms across (a) NPH_{tetra} and (b) $NPH_{trunc-tetra}$. The different colors represent assigned effective charges: $psH_{0.5}$ (purple spheres), psH_1 (green spheres) and $psH_{1.5}$ (orange spheres).

formation for all structures were calculated relative to the total energies of pure elements in their ground states. In the case of γ-Fe_2O_3, the heat of formation -1.4080 eV at^{-1} was determined (with an accuracy of 0.0015 eV at^{-1}, based on basis set convergence tests performed up to a plane wave cut-off energy of 750 eV). The effect of dispersion correction on the heat of formation is discussed in Appendix A. The local charges of ions were analyzed using the method developed by R. Bader and later implemented by Henkelman et al.[81] and Yu et al.[82] This approach defines and separates atoms within a system using zero-flux surfaces, where the charge density reaches a local minimum perpendicular to the surface. To gain insight into the structural properties, the radial distribution function (RDF) was computed. The RDF describes how the atomic density varies as a function of distance from a reference atom. The structural visualization of computational cells was created using the VESTA package.[83]

Results and discussion

Properties of bulk iron oxides

The calculations of bulk iron oxides were carried out to establish a reference for later nanoparticle characterizations, evaluating the surface effects in detail.

Table 1 presents the equilibrium structural characteristics of Fe_3O_4 and γ-Fe_2O_3 bulk phases, including lattice parameters and interatomic distances, along with a comparative analysis against theoretical predictions and experimental results from previous studies. The computed cubic lattice parameter of Fe_3O_4 exhibits excellent agreement across most theoretical methods (with deviations in volume per atom from the experimental data[84] remaining below 1%), except for LDA-based ones.[86] For γ-Fe_2O_3, calculations incorporating the empirically fitted Hubbard $+U$ correction done by other authors[75,89] show a slightly larger deviation of 2%, though this remains within an acceptable accuracy range compared to lattice parameters experimentally derived from XRD patterns[87] reported by Shmakov et al. In magnetite, the interatomic distances for Fe_A–O and Fe_B–O bonds obtained from our DFT calculations show complete uniformity with fixed values of 1.88 Å and 2.06 Å, respectively. This structural consistency is also reflected in the RDF spectrum of maghemite (Fig. 6), where the vacancies within the octahedral sublattice disrupt the well-defined bonding environment, leading to lattice distortions. As a result, the RDF spectrum of γ-Fe_2O_3 displays visibly polydisperse peaks, indicating a broader range of Fe–O bond lengths (1.83–1.92 Å for Fe_A–O and 1.91–2.19 Å for Fe_B–O). The presence of vacancies in the γ-Fe_2O_3 sublattice further modifies the local coordination environment of oxygen atoms. As a result, only 43.8% of oxygen atoms are coordinated by four iron atoms (coordination number CN = 4), compared to 100% in Fe_3O_4. The remaining oxygen atoms are bonded to only three iron atoms (CN = 3). Despite the internal lattice deformation, both bulk structures retain a cubic arrangement with all angles being precisely 90°.

Table 1 Equilibrium characteristics of Fe_3O_4 and γ-Fe_2O_3 bulk structures. The number of iron and oxygen atoms in the unit cell is represented by n. The ground state is represented by lattice parameter a, volume per atom V_{at}, interatomic distance d between tetrahedral Fe_A or octahedral Fe_B iron atoms and oxygen atoms ($Fe_{A/B}$–O) compared with experimental (exp) and theoretical results from the literature. Subscripts min, max and mean denote minimal, maximal and mean values of bond lengths, respectively

Config.	Space group	n Fe	O	a (Å)	V_{at} (Å³ at⁻¹)	V_{at}/V_{exp} (%)	Fe_A–O (Å) d_{min}	d_{max}	d_{mean}	Fe_B–O (Å) d_{min}	d_{max}	d_{mean}	Ref.
Fe_3O_4	$Fd\bar{3}m$	24	32	8.386	10.53	99.6	1.88	1.88	1.88	2.06	2.06	2.06	This work, PBE
		24	32	8.396	10.57	100.0	—	—	—	—	—	—	Exp[84]
		24	32	8.390	10.55	99.8	—	—	1.89	—	—	2.05	GGA + U[85 a]
		24	32	8.387	10.53	99.6	—	—	1.88	—	—	2.06	PBE[74]
		24	32	8.271	10.10	95.5	—	—	1.86	—	—	2.03	LSDA + U[86 b]
γ-Fe_2O_3	$P4_332$	21	32	8.332	10.91	100.0	1.83	1.92	1.86	1.91	2.19	2.03	This work, PBE
		21.3	32	8.347	10.91	100.0	1.84	1.89	1.85	2.01	2.11	2.08	Exp[87]
		21	32	8.335	10.93	100.1	—	—	—	—	—	—	PBE[88]
		21	32	8.395	11.16	102.3	—	—	1.85	—	—	2.04	PBE + U[75 c]
		21	32	8.390	11.14	102.1	—	—	—	—	—	—	PBE + U[89 c]

[a] GGA with Hubbard $+U$ correction (parameter $U_{eff} = 3.8$ eV) using Perdew–Wang 1991 (PW91) exchange–correlation functional. [b] Localized and rotationally invariant version of the local spin density approximation with parameter $U_{eff} = 3.94$ eV. [c] Spin-polarized PBE with Hubbard $+U$ correction (parameter $U_{eff} = 4.1$ eV[75] and 4.3 eV[89]).

21428 | Phys. Chem. Chem. Phys., 2025, **27**, 21424–21440

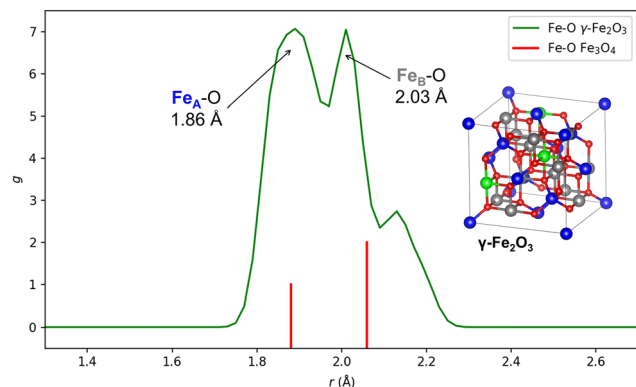This journal is © the Owner Societies 2025

Fig. 6 The partial RDF g for Fe–O in maghemite (γ-Fe$_2$O$_3$) depicted as a green curve. Red vertical markers indicate Fe–O bond distances in magnetite (Fe$_3$O$_4$) for comparison. The function g represents the probability density of finding a particle at the distance r from a reference particle.

Table 2 summarizes the magnetic moments obtained for bulk Fe$_3$O$_4$ and γ-Fe$_2$O$_3$ phases, along with values reported in previous theoretical studies. Both structures were confirmed to have ferrimagnetic ordering, characterized by antiparallel alignment of magnetic moments between iron atoms in the tetrahedral and octahedral sublattices. By integrating the spin density within the PAW spheres surrounding each iron cation, we obtained average magnetic moments of -3.49 μ_B for tetrahedral Fe$_A$ and 3.58 μ_B for octahedral Fe$_B$ iron atoms in Fe$_3$O$_4$. For γ-Fe$_2$O$_3$, the respective values were -3.35 μ_B and 3.66 μ_B. However, comparison with other methods revealed notable discrepancies. In Fe$_3$O$_4$, the computed moment for Fe$_A$ atoms is underestimated by 0.33 μ_B relative to neutron diffraction[93] measurements. For γ-Fe$_2$O$_3$, neutron diffraction[94] experiments report values of -4.18 μ_B for Fe$_A$ and 4.41 μ_B for Fe$_B$, showing the difference of up to 0.83 μ_B from our results. This deviation is primarily due to the excessive delocalization of d-electrons, a well-known feature of transition metal oxides, which challenges

Table 2 Computed magnetic properties of bulk Fe$_3$O$_4$ and γ-Fe$_2$O$_3$ compared with previously computed values from the literature. The μ_{mean} is the average magnetic moment of tetrahedral Fe$_A$, octahedral Fe$_B$ and oxygen atoms. The signs (+) and (−) indicate the spin-up and spin-down orientations of the atomic magnetic moment

| Config. | μ_{mean} (μ_B at^{-1}) | | | Ref. |
	Fe$_A$	Fe$_B$	O	
Fe$_3$O$_4$	-3.49	$+3.58$	$+0.08$	This work, PBE
	-3.47	$+3.58$	$+0.08$	PBE[74]
	-3.41	$+3.49$	$+0.11$	VWN[90 a]
	-4.09	$+3.98$	$+0.03$	PBE + U[74 b]
	-3.68	$+3.62$	$+0.06$	LSDA + U[86]
γ-Fe$_2$O$_3$	-3.35	$+3.66$	$+0.09$	This work, PBE
	-4.01	$+4.13$	$+0.22$	PBE + U[89]
	-4.03	$+4.16$	$+0.14$	GGA + U[91 c]
	-3.50	$+3.73$	$+0.11$	PBE + U[92 b]

[a] LSDA with Vosko–Wilk–Nusair (VWN) parametrization. [b] Spin-polarized PBE with Hubbard +U correction (parameter U_{eff} = 4.0 eV). [c] GGA with Hubbard +U correction (parameter U_{eff} = 4.0 eV).

the accuracy of standard *ab initio* exchange–correlation functionals. Table 2 also highlights that previous studies incorporating the +U correction generally yield more accurate results, although discrepancies with experimentally observed properties still remain. The main challenge of this approach lies in the fact that the effective U parameter (U_{eff}) is empirically fitted to experimental reference data, such as band gaps. Other authors conducting calculations on bulk magnetite and maghemite have employed a wide range of U values, ranging from 3.8 eV[85] to 4.3 eV.[89] Notably, Grau-Crespo *et al.*[91] and Righi *et al.*[92] used the same U parameter for their γ-Fe$_2$O$_3$ calculations and yet obtained significantly different results, with the average magnetic moments differing by 0.53 μ_B for Fe$_A$ and 0.43 μ_B for Fe$_B$. This underscores the inherent limitations of the semi-empirical +U approach, which are even more pronounced in systems where no clear experimental reference is available. This issue is particularly relevant for our nanoparticle models, where surface states, originating from the dangling bonds on surface atoms, modify local electronic structure, introducing in-gap states and shifting band edges. Consequently, the bulk band gap cannot serve as a reliable fitting target, and no other experimental parameters are available for direct validation. Selecting a U_{eff} value without a suitable reference may therefore introduce significant inconsistencies and unphysical results, rather than improve accuracy. Hybrid functionals offer a more rigorous alternative by partially correcting the self-interaction error, but their computational cost is substantial. We successfully performed a single-point HSE06 calculation on bulk γ-Fe$_2$O$_3$ (with PBE-relaxed structure), obtaining magnetic moments of -4.03 μ_B (Fe$_A$) and 4.14 μ_B (Fe$_B$), which more closely match the experimental values. However, due to the high computational demand, we had to restrict the k-point sampling to a single Γ-point and were unable to extend this approach to larger systems, such as our nanoparticle structures. For these reasons, we chose to rely on parameter-free computationally accessible theoretical methods, using the PBE functional, as prior research has shown that the most fundamental magnetic properties – such as spin orientations and relative magnitudes of magnetic moments – are qualitatively well captured in all approaches mentioned above (PBE with and without the +U correction, as well as HSE06). This observation is supported by a comparison of the computed magnetic moment per formula unit (f.u.) for γ-Fe$_2$O$_3$, which in our case is 2.24 μ_B f.u.$^{-1}$ (PBE) and 2.25 μ_B f.u.$^{-1}$ (HSE06), which closely agrees with 2.26 μ_B f.u.$^{-1}$ reported by Sahu *et al.*,[89] who applied an effective parameter U_{eff} = 4.3 eV. Similarly, Bentarcurt *et al.*[75] obtained 2.28 μ_B f.u.$^{-1}$ using the U_{eff} = 4.1 eV correction. In contrast, the experimental value[95] is 2.5 μ_B f.u.$^{-1}$

Additional properties of bulk γ-Fe$_2$O$_3$, including Bader charge analysis and formation enthalpy, were also determined and are further presented in Table 3. The results indicate that charge transfer is also influenced by the local coordination environment. Specifically, iron atoms exhibit greater electron transfer as their coordination increases from tetrahedral to octahedral, with a charge difference of 0.0956 e. A similar trend is observed for oxygen, where charge transfer varies by 0.0798 e

This journal is © the Owner Societies 2025

Phys. Chem. Chem. Phys., 2025, **27**, 21424–21440 | **21429**

Table 3 Additional computed properties for bulk γ-Fe_2O_3. CN denotes the coordination number, representing the number of nearest neighbors for each atomic site. q represents the average effective atomic charge values obtained from Bader charge analysis for tetrahedral Fe_A, octahedral Fe_B and O atoms. The signs (+) and (−) associated with this parameter indicate the increase and decrease in electron density, respectively. The heat of formation $\Delta_f H$ was calculated at 0 K

Config.	Site	CN	q (e)	$\Delta_f H$ (eV at^{-1})	$\Delta_f H$ (kJ mol^{-1})
γ-Fe_2O_3	Fe_A	4	−1.5631	−1.4080	−679.26
	Fe_B	6	−1.6587		
	O	3	+1.0297		
		4	+1.1095		

between the threefold- and fourfold-coordination sites. γ-Fe_2O_3 is classified as a charge transfer insulator,[91] where the electronic structure reflects the redistribution of charge, leading to the formation of Fe^{3+} and O^{2-} species. The valence band is primarily composed of occupied O 2p states, while the bottom of the conduction band is dominated by unoccupied Fe 3d levels. The resulting band gap inhibits spontaneous electron migration from oxygen back to iron atoms, thereby limiting electronic conductivity under normal conditions. Our analysis supports this behavior by confirming the distinct charge transfer from Fe to O that characterizes its insulating nature.

The formation enthalpy of γ-Fe_2O_3 was determined to be −679.26 kJ mol^{-1}, which is underestimated compared to results obtained from earlier theoretical[92] and experimental[96] studies by 3.5% and 4.5%, respectively, but still remains in reasonable agreement.

Structural characteristics of nanoparticle models

Nanometre-sized IONPs containing tens to several hundreds of atoms, such as our models, lack well-defined lattice parameters and a bulk-like center. Surface effects, shape anisotropy and differences in atomic positions compared to the bulk further enhance their structural distinction. Additionally, the models constructed for this study exhibit a core–shell architecture, with tetrahedral Fe_A atoms occupying positions near the center. This structural design stems from the assumption[97] that Fe_A atoms lack stability at the nanoparticle surfaces due to insufficient coordination, potentially leading to their rearrangement into octahedral positions. The interatomic distances summarized in

Table 4 provide insight into the bonding environment, as further visualized by the RDF spectra in Fig. 7 and 8.

The NP$_{tetra}$ and NP$_{trunc-tetra}$ models show significant structural distortions due to the exposure to vacuum conditions. Without additional external stabilization, the surface O atoms become undercoordinated with unsaturated valencies, leading to shorter and stronger bonds. This effect is particularly evident in O$_{edge}$ atoms, which are bonded to only one Fe_B atom, resulting in a mean Fe_B–O$_{edge}$ bond length 0.46 Å shorter than Fe_B–O in bulk Fe_3O_4. A similar, though visibly less pronounced, trend is observed for O$_{facet}$ atoms coordinated by two or three Fe_B atoms. The subsurface layer also adapts to the surface-induced constraints and regularly ordered core, with bond elongation serving as a compensatory mechanism. This is reflected in Fe_B–O$_{inner}$ bonds, which extend up to 2.40 Å in NP$_{tetra}$ and 2.39 Å in NP$_{trunc-tetra}$. Despite the differences between the tetrahedral and truncated tetrahedral models, which belong to the same class of polyhedral structures, the overall bond lengths remain consistent.

The stabilization of dangling bonds using psH atoms compensates surface charge in a controlled manner, reducing bond length deviations and promoting a more uniform distribution of values within the 1.89–2.24 Å range for NPH$_{tetra}$ and the 1.88–2.20 Å range for NPH$_{trunc-tetra}$. The RDF spectra for both structures indicate that interatomic distances approaching the upper limit of the mentioned intervals (2.24 Å and 2.20 Å) are present at an insignificant frequency compared to the reference mean values for each coordination type. Additionally, compared to bulk Fe_3O_4, the mean Fe_B–O$_{edge/facet/inner}$ bond lengths show a slight contraction.

Based on these observations, it is reasonable to expect a uniformity in O–psH$_x$ bond lengths across different charge states (x = 0.5, 1 or 1.5), as this would indicate that our method, based on chemical ECR principle, effectively stabilizes the surfaces and ensures a consistent structural response to the variations in charge. Indeed, our results mostly support this expectation: the O–H$_{1.0}$ bond lengths range from 0.97 to 0.98 Å, with the O–H$_{1.0}$ and O–H$_{1.5}$ distances being nearly identical (differing by only 0.01–0.02 Å). In contrast, the O–H$_{0.5}$ bonds are noticeably elongated by 0.09 Å, which may reflect a different level of local charge compensation.

Our results highlight the critical role of surface capping and full structural relaxation, as undercoordinated surface atoms undergo substantial displacements that propagate into the

Table 4 Interatomic distances d between tetrahedral Fe_A or octahedral Fe_B atoms and oxygen atoms ($Fe_{A/B}$–O) in NP$_{tetra}$, NPH$_{tetra}$, NP$_{trunc-tetra}$ and NPH$_{trunc-tetra}$. The subscripts min, max and mean denote the minimal, maximal and mean bond lengths, respectively. The subscripts edge and facet refer to oxygen atoms positioned at the edges and facets of the nanoparticles, while O$_{inner}$ describes oxygen atoms located within the structure. The n_{surf} represents the number of atoms in the surface layer and n is the total number of atoms

Config.	n_{surf}	n_{surf}/n (%)	Fe_A–O$_{inner}$ (Å) d_{min}	d_{max}	d_{mean}	Fe_B–O$_{inner}$ (Å) d_{min}	d_{max}	d_{mean}	Fe_B–O$_{facet}$ (Å) d_{min}	d_{max}	d_{mean}	Fe_B–O$_{edge}$ (Å) d_{min}	d_{max}	d_{mean}
NP$_{tetra}$	96	59.6	1.79	1.88	1.86	1.94	2.40	2.09	1.72	2.04	1.85	1.58	1.62	1.60
NPH$_{tetra}$		37.4	1.89	1.97	1.92	1.92	2.24	1.99	1.90	2.04	1.94	1.91	2.00	1.96
NP$_{trunc-tetra}$	84	57.9	1.77	1.88	1.85	1.94	2.39	2.08	1.73	2.02	1.84	1.58	1.61	1.60
NPH$_{trunc-tetra}$		36.7	1.88	1.95	1.92	1.91	2.12	1.96	1.89	2.13	1.94	1.93	2.20	1.98

21430 | *Phys. Chem. Chem. Phys.*, 2025, **27**, 21424–21440

This journal is © the Owner Societies 2025

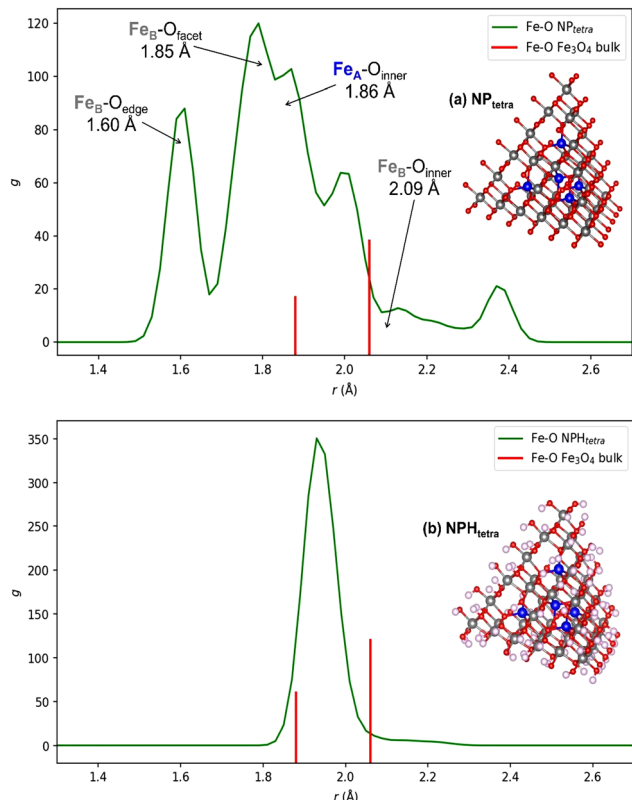**Fig. 7** The partial RDF g for Fe−O in (a) NP_{tetra} and (b) NPH_{tetra} shown as a green curve. Red vertical markers indicate Fe−O bond distances in magnetite (Fe_3O_4) bulk for comparison. The numerical values in the RDF spectrum of NP_{tetra} represent average interatomic distances between Fe and O at different coordination sites within the nanoparticle.
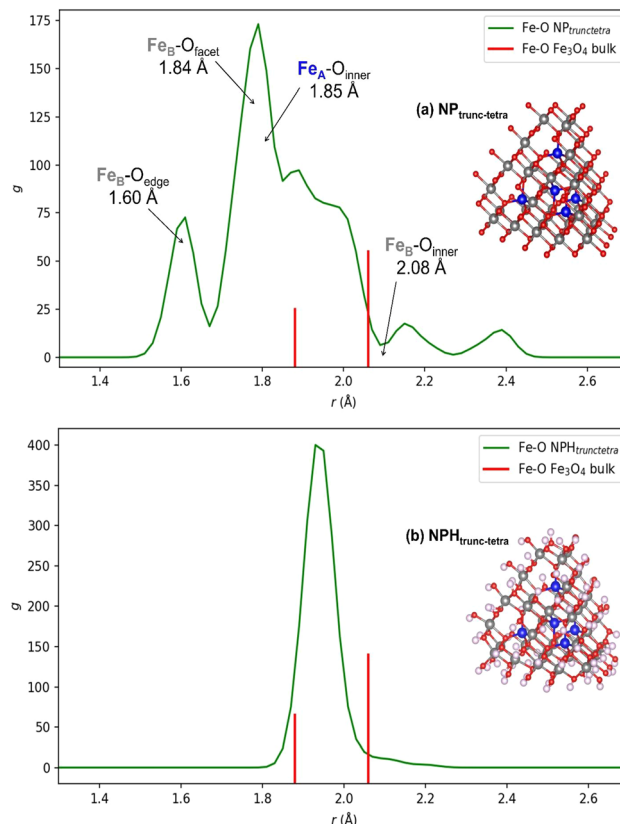

Fig. 8 The partial RDF g for Fe−O in (a) $NP_{trunc-tetra}$ and (b) $NPH_{trunc-tetra}$ shown as a green curve. Red vertical markers indicate Fe−O bond distances in magnetite (Fe_3O_4) bulk for comparison. The numerical values in the RDF spectrum of $NP_{trunc-tetra}$ represent average interatomic distances between Fe and O at different coordination sites within the nanoparticle.

subsurface layer. For this reason, static calculations constrained to bulk-like interatomic distances would easily oversimplify the system and fail to capture the true impact of surface distortions on properties such as atomic-scale magnetism.

Magnetic properties of iron atoms in the nanoparticle models

The most stabilized magnetic configurations of NP_{tetra}, NPH_{tetra}, $NP_{trunc-tetra}$ and $NPH_{trunc-tetra}$ obtained from our calculations are depicted in Fig. 9. For better visualization, each structure is divided into three hypothetical shells: (C) the tetrahedral Fe_A sublattice, situated in the core part of the nanoparticle model and two separate regions of the octahedral Fe_B sublattice, with iron atoms located in the facets (F) and at the edges (E) of the subsurface layer.

We did not manage to stabilize ferrimagnetic ordering in the NP_{tetra} and $NP_{trunc-tetra}$. Instead, a spin-flipping phenomenon was observed in both the Fe_A and Fe_B sublattices, leading to an alternative, more complex magnetic arrangement that deviates from the expected bulk-like state. A similar effect was reported by López et al.,[51] where a spin–flip occurred in a tetrahedral Fe_A atom positioned at the center of an isolated cage-like $Fe_{17}O_{16}$ cluster. In both our non-functionalized models, multiple spin-flips coexist simultaneously; however, one of them also involves

a Fe_A atom located in the center of the nanoparticle, as shown in Fig. 9 for both $(C)NP_{tetra}$ and $(C)NP_{trunc-tetra}$. In contrast to the additional findings of López et al.,[51] where the magnitudes of Fe_A and Fe_B magnetic moments in a larger (over 100-atom) spherical $Fe_{45}O_{68}$ cluster deviated by less than 0.25 μ_B from those found in bulk Fe_3O_4, we observe an anisotropic magnetic behavior, linked to the symmetry of the tetrahedral and the truncated tetrahedral structures. Fig. 10 illustrates how the absolute value of the magnetic moment of iron atoms in NP_{tetra} decreases in discrete steps with increasing distance from the nanoparticle center, reflecting the non-equivalent positions of Fe atoms within the structure. A similar trend is also observed for $NP_{trunc-tetra}$; however, as shown in Table 5, in this geometry, there are only five structurally and magnetically non-equivalent groups of iron atoms, compared to the six present in NP_{tetra}. The spin-flipping processes, combined with the reduced magnetic moments, result in a decrease in the total magnetization per nanoparticle (M_{NP}) by 87% and 89% for NP_{tetra} and $NP_{trunc-tetra}$, respectively, relative to the calculated bulk-like reference M_B values (determined for the nanoparticle stoichiometries using the average magnetic moments of Fe_A, Fe_B and O atoms from our calculations of bulk γ-Fe_2O_3). Factors such as reduced M_{NP} values and spin-flipping (previously used in collinear
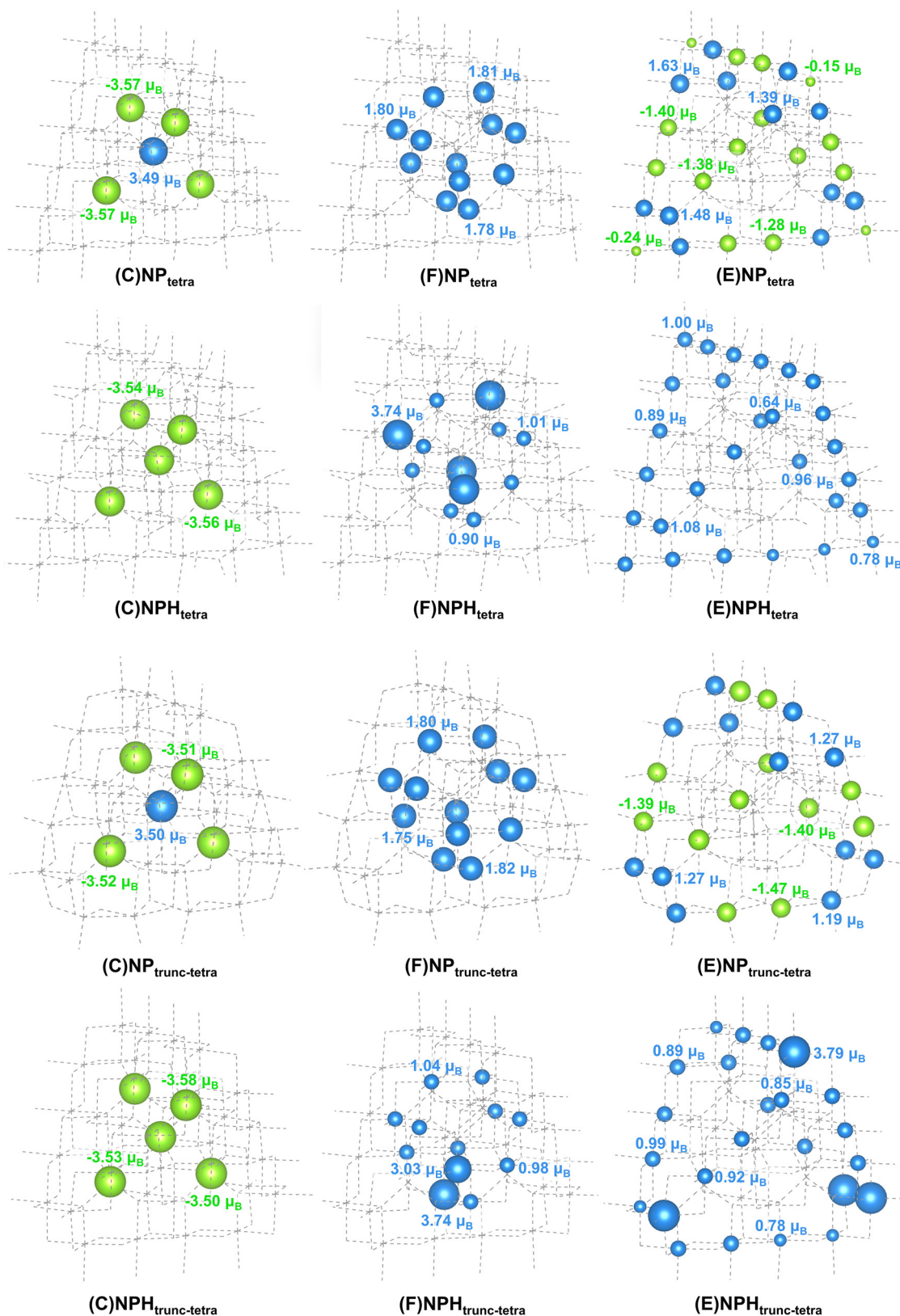
This journal is © the Owner Societies 2025

Phys. Chem. Chem. Phys., 2025, **27**, 21424–21440 | **21431**

Fig. 9 The magnetic arrangement of NP$_{tetra}$, NPH$_{tetra}$, NP$_{trunc-tetra}$ and NPH$_{trunc-tetra}$, showing only iron atoms. The grey dashed lines represent Fe–O bonds. Shell (C) represents the tetrahedral Fe$_A$ sublattice, while shells (F) and (E) correspond to octahedral Fe$_B$ atoms located in the facets and at the edges of the subsurface layer, respectively. Green and blue spheres indicate spin-down (↓) and spin-up (↑) orientation of atomic magnetic moment, respectively. The spin-down (↓) orientation corresponds to the minority spin. The size of each iron sphere is directly proportional to the absolute value of its magnetic moment.
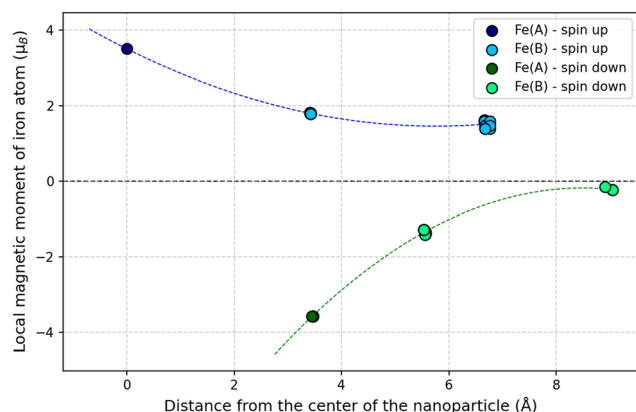
21432 | *Phys. Chem. Chem. Phys.*, 2025, **27**, 21424–21440

This journal is © the Owner Societies 2025

Fig. 10 Dependence of the magnitude of the magnetic moment on the distance of tetrahedral Fe_A and octahedral Fe_B iron atoms from the center of NP_{tetra}. The dashed lines are included merely to guide the eye and do not represent interpolated data.

Table 5 The average magnetic moments μ_{mean} of structurally non-equivalent Fe sites in the lowest energy magnetic configuration of NP_{tetra}, NPH_{tetra}, $NP_{trunc-tetra}$ and $NPH_{trunc-tetra}$. The values are further separated by spin orientation (spin-down (↓) and spin-up (↑))

Fe site			μ_{mean} (μ_B at^{-1})			
			NP_{tetra}	NPH_{tetra}	$NP_{trunc-tetra}$	$NPH_{trunc-tetra}$
Core (Fe_A)	(C)	↑	3.498	—	3.495	—
		↓	−3.565	−3.549	−3.512	−3.539
Facet (Fe_B)	(F)	↑	1.797	1.001	1.788	0.999
				3.730		3.388
Edge (Fe_B)	(E)	↑	1.512	0.899	1.243	0.884
						3.760
		↓	−1.338	—	−1.409	—
Vertex (Fe_B)	(E)	↑	—	0.895	—	—
		↓	−0.214	—	—	—

magnetism calculations employed by Bianchetti *et al.*[98] to mimic spin-canting processes) are significant indicators of a magnetically disordered surface layer. Eddahri *et al.*[99] reported a reduction in surface magnetization M_{surf} by approximately 81% compared to the value predicted for perfect ferrimagnetic order, along with a decrease in the total magnetization M_{NP} by around 29% for a 5 nm cubic-shaped magnetite nanoparticle under vacuum conditions, simulated by Monte Carlo methods. These findings, in agreement with our results, support the observation that magnetization M_{NP} significantly decreases with decreasing size of the nanoparticle. Given the nanometre-scale dimensions of our models, it is more appropriate to describe the entire structure as magnetically disordered, as our M_{NP} values are comparable to the M_{surf} reported in ref. 99. In fact, 59.6% and 57.9% of atoms in NP_{tetra} and $NP_{trunc-tetra}$, respectively, are located in the surface layer, thereby enhancing surface-related magnetic effects and suppressing the emergence of a distinct magnetic core. Deviations from the expected ferrimagnetic ordering can be attributed to the cleavage of surface Fe–O bonds, which disrupts the superexchange interactions between neighboring iron atoms mediated by oxygen. Additional distortions in interatomic

Table 6 All calculated ferrimagnetic (FerriM) and spin–flip (SpinF) configurations for nanoparticle models and bulk γ-Fe_2O_3, reported with the corresponding numbers of spin-flipped atoms n_{SF} in the tetrahedral Fe_A and octahedral Fe_B sublattices. M_{NP} and M_{cell} denote the total magnetization per nanoparticle and per unit cell (for bulk), respectively. Relative energies E_{rel} are given with respect to the lowest energy states

Config.	Ordering	n_{SF}		$M_{NP/cell}$	E_{rel}
		Fe_A	Fe_B	(μ_B)	(eV)
NP_{tetra}	SpinF	1	16	18.4	0.00
$NP_{trunc-tetra}$	SpinF	1	12	13.3	0.00
NPH_{tetra}	FerriM	0	0	30.3	0.00
	SpinF	1	13	6.4	1.02
$NPH_{trunc-tetra}$	FerriM	0	0	32.7	0.00
	SpinF	1	11	3.2	0.70
Bulk γ-Fe_2O_3	FerriM	0	0	23.7	0.00
C1	SpinF	2	4	4.1	3.11
C2	SpinF	2	4	6.7	2.84
C3	SpinF	1	2	13.9	1.60
C4	SpinF	2	5	4.3	2.85

distances (see Fig. 7(a) for NP_{tetra} and Fig. 8(a) for $NP_{trunc-tetra}$) and angles influence these interactions by changing the overlap between Fe 3d and O 2p orbitals, thereby directly affecting the strength of exchange coupling. As a result, the system tends to minimize its local exchange energy through magnetic frustration, which manifests as the spin-flipping phenomenon, particularly under the collinearity constraints imposed during calculations. The flow of additional charge from psHs to surface oxygen atoms helps to preserve the antiparallel alignment of the Fe_A and Fe_B sublattices, resulting in the lowest energy configuration with ferrimagnetic ordering (see the relative energies in Table 6). This additional surface bonding stabilizes the Fe–O interatomic distances close to the bulk results (shown in Fig. 7(b) for NPH_{tetra} and in Fig. 8(b) for $NPH_{trunc-tetra}$) and enhances the ferromagnetic superexchange within the Fe_B sublattice, compared to the non-functionalized models. Nevertheless, M_{NP} still remains significantly reduced by 78% and 73% for NPH_{tetra} and $NPH_{trunc-tetra}$, respectively, relative to the estimated M_B values (all M_{NP} are reported in Table 6). This ongoing decrease in M_{NP}, despite the preservation of bulk-like spin alignment, can be linked to variations in the magnitudes of atomic magnetic moments, with some moments substantially quenched compared to bulk. This trend is consistently observed across all nanoparticle models, as exemplified by values −0.24 μ_B in NP_{tetra} and 0.64 μ_B in NPH_{tetra} (Fig. 9), and likely reflects altered intra-atomic exchange interactions, although a detailed understanding of this mechanism lies beyond the scope of the present study. Importantly, surface capping with psH atoms appears to restore the tetrahedral sublattice located at the center of the nanoparticle to a magnetic state more closely resembling that of the bulk (see Fig. 9 for both (C)NPH_{tetra} and (C)$NPH_{trunc-tetra}$).

The difference in M_{NP} between the lowest energy states of the functionalized and non-functionalized NP models reaches 9% for the tetrahedral and 16% for the truncated tetrahedral geometry, highlighting the notable impact of surface coating on
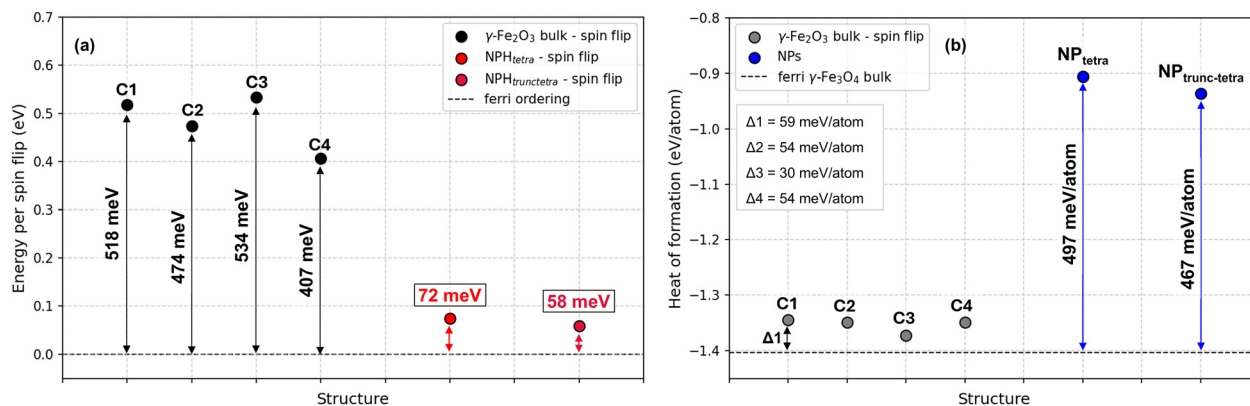
This journal is © the Owner Societies 2025

Phys. Chem. Chem. Phys., 2025, **27**, 21424–21440 | **21433**

Fig. 11 Dependence of (a) energy per spin–flip and (b) heat of formation on the analyzed structures. Energies account for full structural relaxation. Configurations C1–C4 represent additional magnetic orderings of bulk γ-Fe$_2$O$_3$ with different distributions of spin-flipped Fe atoms. In (a), the energies are shown relative to the ferrimagnetic ground state (dashed line) for both bulk γ-Fe$_2$O$_3$ and NP models. In (b), the calculated heats of formation are plotted and the energy differences relative to the bulk ferrimagnetic ground state are also indicated ($\Delta 1$–$\Delta 4$ for configurations C1–C4).

the magnetic moments. These differences may have a limited impact on experimentally observed properties of ultra-small nanoparticles, due to the presence of a magnetically disordered layer (dependent on surface morphology[100]), which has been reported to reach approximately 0.9 nm[101] in thickness. For NPs smaller than 3 nm, this disordered layer is associated with saturation magnetization values of zero or near zero.[53,102] In contrast, it may become increasingly more relevant in larger nanoparticles, where the magnetic core contributes more substantially to the overall behavior.

Even though the ferrimagnetic configuration is identified as the lowest energy structure for the functionalized models, the final magnetic ordering obtained during synthesis may be influenced by various factors – especially when possible energetically accessible local minima lie close to the global minimum. To address this, we performed a comparative analysis of spin–flip energetics and heats of formation, as shown in Fig. 11. We began by computing additional metastable NPH structures featuring spin–flip distributions similar to those observed in the non-functionalized NP models, but exhibiting significantly lower M_{NP} values (reduced by 12.0 μ_B and 10.1 μ_B compared to NP$_{tetra}$ and NP$_{trunc-tetra}$, respectively). The relative energies (E_{rel}) of these spin-flipped configurations, calculated

with respect to the ferrimagnetic ground state, incorporating both the magnetic rearrangement and structural relaxation, are presented in Table 6. To further investigate the stability of spin disorder, we also extended this approach to bulk γ-Fe$_2$O$_3$ by generating four distinct magnetic configurations (C1–C4) with varying distributions and numbers of spin-flipped Fe atoms in the tetrahedral and octahedral sublattices. C1 and C2 contain six flipped spins, while C3 includes only three and C4 comprises seven (the respective spin arrangements are visualized in Fig. 12). For C1–C4, the energy per spin–flip falls within the range of 407–534 meV, confirming that spin-flipping is energetically not favorable in the bulk, with ferrimagnetic ordering remaining highly stable. In contrast, in the anisotropically shaped NPs, the cost of a single flipped spin is substantially lower than in the bulk, with values of 72 meV for NPH$_{tetra}$ and 58 meV for NPH$_{trunc-tetra}$. This suggests increased magnetic softness and a higher probability of spin disorder. It is also important to note that our results were obtained at temperatures of 0 K, so the higher energy states with flipped spins may become accessible under synthesis conditions. At 300 °C (a commonly used temperature for polyhedral IONPs preparation), the energy contribution from thermal fluctuations is approximately 50 meV, which is comparable to the spin–flip barriers computed for these nanostructures. When combined with other factors, such as internal distortions and the kinetic effect of rapid growth, this supports the plausibility of the spin-disordered layer forming under realistic conditions. The heats of formation obtained for NP models without psHs atoms at the surfaces (NP$_{tetra}$ and NP$_{trunc-tetra}$) are visibly less negative than for bulk γ-Fe$_2$O$_3$, differing by 495 and 467 meV per atom, respectively. This extensive energy difference primarily reflects the cost of surface formation. In comparison, the contribution from spin-flipping is minimal, further supporting the possibility of spin disorder forming naturally as the nanoparticle structure evolves.

It is also important to consider that different capping groups can introduce varying effective charges, thereby influencing the energy associated with spin-flipping. In this study, we
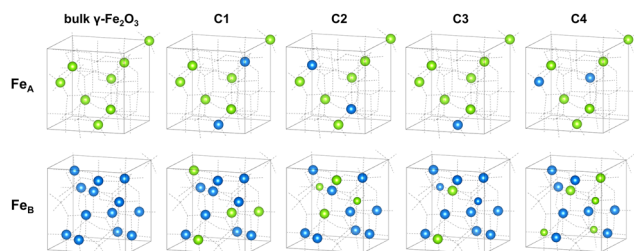

Fig. 12 The magnetic arrangement of C1–C4 configurations, showing only iron atoms. The grey dashed lines represent Fe–O bonds. Green and blue spheres indicate spin-down ($\downarrow$) and spin-up ($\uparrow$) orientation of the atomic magnetic moment, respectively. The size of each iron sphere is directly proportional to the absolute value of its magnetic moment.

21434 | *Phys. Chem. Chem. Phys.*, 2025, **27**, 21424–21440

This journal is © the Owner Societies 2025

employed effective charge values designed to fully compensate for the disruptions in the Fe–O bonding network at the NP surfaces. On that note, Bianchetti et al.[98] carried out calculations by applying various ligands to the corner and on the facet of a cubic magnetite IONP, analyzing the spin–flip energetics for a single octahedral iron atom. Their results showed that these energies vary widely from −15 meV/114 meV (ethanol) to 141 meV/280 meV (acetic acid) for local high coverage of ligands. The spin–flip energies for our psH-capped NPs are more consistent with their results for the non-bridging ligand, which is expected, as each surface oxygen atom in our models is capped individually by a psH species.

Magnetic properties of oxygen atoms in the nanoparticle models

The overall M_{NP} of the nanoparticles is determined not only by the magnetic moments of iron atoms, but also by contributions from oxygen atoms, which play a crucial role – particularly in the non-functionalized models, where a pronounced scattering of magnetic moments is observed (see Fig. 13(a)). In NP_{tetra}, the largest magnetic moments were 0.447 μ_B and 0.264 μ_B for oxygen atoms located at the edges (O_{edge}) and on the facets (O_{facet}) of the NP, respectively. This value for O_{facet} (oxygen coordinated by two or three iron atoms) correlates well with the absolute values of 0.244 μ_B (SGGA) and 0.300 μ_B (SGGA + U) reported earlier by Palotás et al.[50] for oxygen atoms with the same coordination environment in a $Fe_{25}O_{30}$ cluster. Righi et al.[92] also measured magnetic moments of 0.250 μ_B for this type of coordination. These results indicate that the deviations in magnetic moments, relative to the average value of 0.09 μ_B in bulk γ-Fe_2O_3, arise from the reduced coordination of surface oxygen atoms. Cleavage of Fe–O bonds redistributes electron density around oxygen atoms, possibly enhancing their spin polarization, which leads to induced magnetic moments quantified within DFT by integrating the difference between spin-up and spin-down electron densities. Spin-flipping in O atoms is also observed to a non-negligible extent across all NP models. The associated changes in electron distribution are further examined through charge transfer processes revealed by Bader analysis.

Fig. 14(a) shows that O_{inner} atoms (bound to four Fe atoms) receive a similar amount of charge from the surrounding iron atoms as in bulk γ-Fe_2O_3, differing on average by 0.14 e. This is also reflected in their absolute magnetic moments, which, for distances smaller than 4 Å from the center of the NP, closely match the bulk values. Four additional O_{inner} atoms are located farther than 5 Å from the nanoparticle center, positioned closer to the vertices of the NP where surface effects become more pronounced, and both their magnetic moments and transferred charge begin to deviate accordingly. In contrast to the values obtained for O_{inner}, the transferred charge to O_{facet} atoms ranges from 0.63 to 0.77 e, while for O_{edge} atoms (coordinated by only one Fe atom), the entire range shifts to lower values, spanning from 0.36 to 0.42 e. This trend highlights the decreasing charge transfer associated with decreasing coordination number – a behavior already observed in bulk γ-Fe_2O_3 (Table 3),
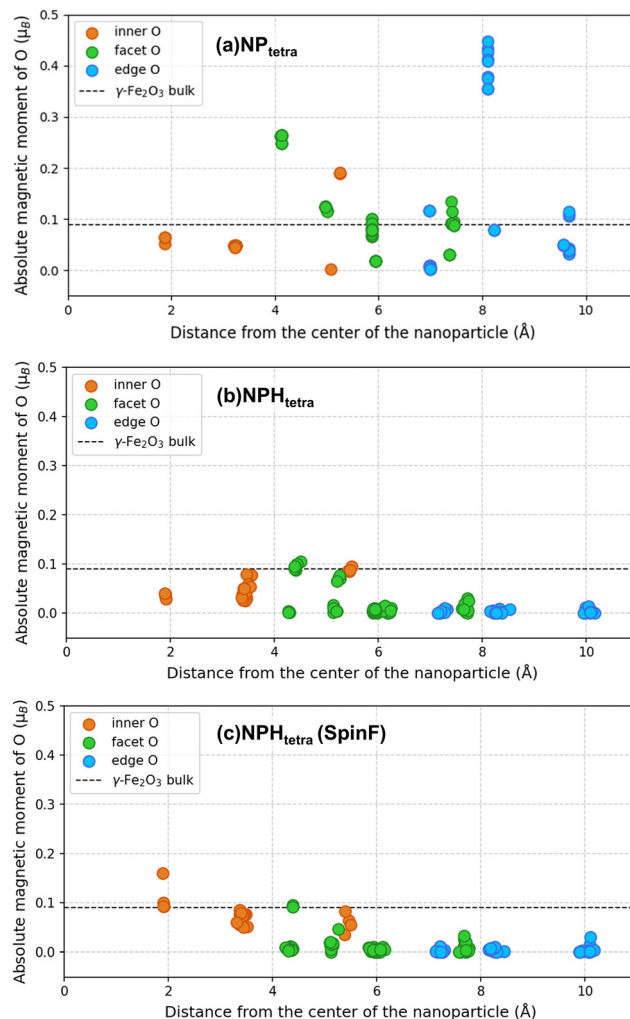

Fig. 13 Dependence of the absolute magnetic moment of oxygen atoms on their distance from the center of nanoparticles: (a) NP_{tetra}, (b) NPH_{tetra} and the metastable (c) NPH_{tetra} with spin-flipping in both iron sublattices. Oxygen atoms located on the inside (O_{inner}), on the facets (O_{facet}) and at the edges (O_{edge}) of the NP models are color-coded accordingly. The dashed line represents the bulk γ-Fe_2O_3 reference value.

though with much smaller differences. Functionalization of surface oxygen atoms with psHs shifts the charge transfer values closer to those observed in bulk, particularly for O_{inner} and O_{facet} (as shown in Fig. 14(b)). O_{facet} atoms are capped with psH atoms carrying effective charges of 0.5 or 1.0, compared to 1.5 for O_{edge}. Our results show that the highest assigned charge, intended to compensate for the loss of three Fe–O bonds, does not fully restore the bulk electron distribution, as the charge transferred to O_{edge} atoms remains within 0.55–0.68 e, still differing on average by 0.49 e from the bulk. Additional Bader analysis revealed, that the average transferred charge from psH atoms to oxygen is 0.33 e for $psH_{1.5}$, 0.60 e for psH_1 and 0.50 e for $psH_{0.5}$, indicating that only the latter fully transfers its nominal charge. This may also explain the elongation of O–$psH_{0.5}$ bonds compared to O–$psH_{1.5/1.0}$, as previously discussed in the section on the structural properties of the nanoparticle models. Even with these discrepancies in charge transfer
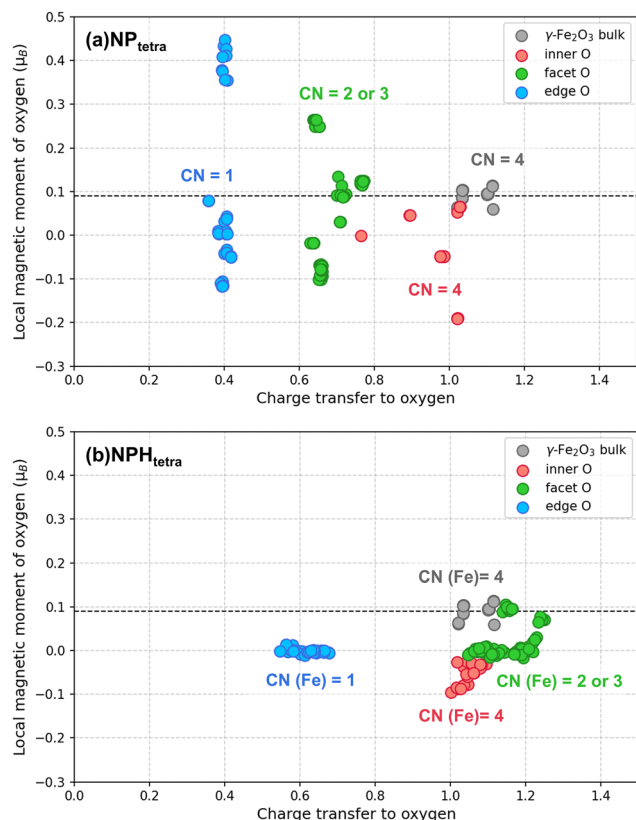
This journal is © the Owner Societies 2025

Phys. Chem. Chem. Phys., 2025, **27**, 21424–21440 | **21435**

Fig. 14 Dependence of the local magnetic moment of oxygen on charge transfer to oxygen from iron atoms in (a) NP_{tetra} and from both iron and psH atoms in (b) NPH_{tetra}. Oxygen atoms located on the inside (O_{inner}), on the facets (O_{facet}) and at the edges (O_{edge}) of the NP models are color-coded accordingly.

($psH_{1.0}$ gives more than $psH_{1.5}$), the functionalization still appears to stabilize magnetic interactions. None of the O_{facet} or O_{edge} atoms exhibit absolute magnetic moments exceeding 0.105 μ_B, and in several cases, particularly among O_{edge} sites, the spin polarization is entirely quenched resulting in a zero atomic magnetic moment (see Fig. 13(b)). A comparison between the NPH_{tetra} and NPH_{tetra} (SpinF) configurations demonstrates that the spin-flipping within the Fe sublattices has a negligible impact on the local magnetic moments of oxygen atoms. As shown in Fig. 13(b) and (c), the absolute magnetic moments remain almost unchanged across the two configurations. This suggests that the dominant factor governing oxygen magnetization is charge transfer associated with the coordination environment, rather than the spin arrangement of iron atoms.

It is also important to note that the same trends observed in the tetrahedral configurations were consistently reproduced in the nanoparticles with truncated tetrahedral geometry, making a separate discussion of these results unnecessary.

Conclusions

In this work, we investigated how tetrahedral and truncated tetrahedral morphologies influence the structural and

magnetic properties of nanometre-sized iron oxide nanoparticles using density functional theory. Both polyhedral shapes were studied in non-functionalized form and also with surfaces passivated by psH_x atoms with different effective charges (x = 0.5, 1.0 or 1.5). While these simplified surface terminations do not fully capture the chemical complexity of real ligands, they provide valuable insight into the key factors influencing the behavior of such nanostructures.

The outcomes reveal that non-functionalized NPs undergo significant surface-induced distortions. The undercoordination influences the strength of superexchange interactions, alters charge transfer processes and ultimately disrupts ferrimagnetic ordering characteristic for bulk magnetite and maghemite. For the tetrahedral morphology, Fe–O bonds at the nanoparticle edges are shortened by up to 0.46 Å, while oxygen atoms exhibit elevated magnetic moments reaching up to 0.447 μ_B. These changes lead to spin-flipping processes in both the tetrahedral and octahedral iron sublattices, resulting in an almost 90% reduction in total magnetization. The surface passivation with psH atoms weakens these effects by saturating the dangling bonds formed upon cleavage, compensating for the unsatisfied valencies. In both functionalized models, Fe–O bond lengths become more uniform and closer to bulk values, as confirmed by RDF analysis. Ferrimagnetic ordering emerges as the energetically preferred configuration, in contrast to the alternative containing spin flipping. The total magnetization of the capped nanoparticle M_{NP} increases slightly, by 9% for the tetrahedral and 16% for the truncated tetrahedral geometry. However, the overall magnetization is still substantially reduced compared to the estimated bulk-like values, primarily due to residual quenching of atomic magnetic moments in subsurface iron atoms (as low as –0.24 μ_B in NP_{tetra} and 0.64 μ_B in NPH_{tetra}).

Spin–flip energetics supports the emergence of magnetically disordered structures under realistic conditions. The average energy cost per single spin–flip was calculated to be 72 meV for NPH_{tetra} and 58 meV for $NPH_{trunc-tetra}$, which is substantially lower than the 407–534 meV/spin–flip observed in metastable bulk γ-Fe_2O_3 configurations.

Charge transfer analysis demonstrates that oxygen atoms in different coordination environments exhibit distinct behavior. In the non-functionalized NP_{tetra} model, oxygen atoms located at the edges receive only 0.36–0.42 e from neighboring iron atoms, while those in the facets receive 0.63–0.77 e, reflecting a trend of decreasing charge transfer with lower coordination number. Upon the functionalization, charge transfer to oxygen atoms located in the facets in NPH_{tetra} increases to 1.05–1.25 e, more resembling bulk-like values. Although the $psH_{1.5}$ group gives less than half of its nominal charge – resulting in reduced charge transfer to oxygen atoms located at the edges of NPH_{tetra} – this capping method still helps to stabilize the local electronic environment.

Beyond the immediate significance of our results, this study also demonstrates a novel use of a pseudo-hydrogen passivation scheme to model surface capping on iron oxide nanoparticles. This method offers a computationally accessible strategy that may prove broadly useful for future simulations

21436 | *Phys. Chem. Chem. Phys.*, 2025, **27**, 21424–21440

This journal is © the Owner Societies 2025

Table 7 The heat of formation $\Delta_f H$, average magnetic moments μ_{mean} of tetrahedral Fe_A, octahedral Fe_B and oxygen O atoms and the lattice parameter a of bulk γ-Fe_2O_3 calculated using three approaches: the standard PBE exchange–correlation functional, the PBE functional with DFT-D3 dispersion correction and the PBE functional with DFT-D3 Becke–Johnson (BJ) damping variant. $\Delta_f H / \Delta_f H_{exp}$ and a/a_{exp} denote deviations from experimental formation enthalpy and lattice parameter, respectively

Method	$\Delta_f H^a$		$\Delta_f H / \Delta_f H_{exp}$	μ_{mean} (μ_B at^{-1})			a	a/a_{exp}
	eV at^{-1}	kJ mol^{-1}	(%)	Fe_A	Fe_B	O	(Å)	(%)
Standard PBE	−1.4080	−679.26	4.5	−3.35	+3.66	+0.09	8.3317	0.2
PBE with DFT-D3	−1.4199	−684.99	3.7	−3.33	+3.65	+0.09	8.3013	0.6
PBE with DFT-D3 (BJ)	−1.4361	−692.84	2.6	−3.31	+3.64	+0.09	8.2789	0.8

^{a} Heats of formation were calculated with respect to the equilibrium elemental reference states (bcc Fe and O_2 molecule) using the same computational approach.

of magnetic nanomaterials. Looking ahead, the framework established here could be extended to larger and more complex nanoparticle morphologies by integrating machine-learned potentials trained on quantum-mechanical data. However, such extensions remain beyond the scope of the present work, as reliable machine-learning models capable of capturing complex magnetic interactions with high accuracy are still under active development.

Author contributions

V. B.: investigation, writing – original draft, writing – review & editing, visualization, data curation. M. F.: conceptualization, supervision, methodology, resources, writing – review & editing. N. P.: funding acquisition, project administration, writing – review & editing. J. P.: conceptualization, supervision, methodology, writing – review & editing.

Conflicts of interest

There are no conflicts to declare.

Data availability

The computational details (corresponding to structures from Fig. 3) are available at Zenodo at **https://doi.org/10.5281/zenodo.15207977**.

Appendix A

The influence of dispersion corrections, using the DFT-D3 method of Grimme et al.[103] and its Becke–Johnson (BJ) damping variant,[104] was evaluated by comparing the calculated heats of formation, lattice parameters and magnetic moments of bulk γ-Fe_2O_3. The results are summarized in Table 7.

Including dispersion corrections reduces the error in the calculated heat of formation ($\Delta_f H$) of bulk γ-Fe_2O_3 relative to the experimental data. While standard PBE functional yields a deviation of 4.5%, applying the DFT-D3 correction lowers this deviation to 3.7%, and the Becke–Johnson (BJ) damping variant further improves the agreement to 2.6%. However, this enhanced thermochemical accuracy is accompanied by an increased discrepancy in structural parameters – the lattice

constant a becomes progressively underestimated, with the BJ-corrected value deviating by 0.8% from experiment. Notably, while the DFT-D3 (BJ) correction improves $\Delta_f H$ accuracy by 1.9% relative to PBE, it also induces a 1.9% contraction in the atomic volume, reflecting a denser lattice.

Given that our study focuses primarily on relative energy differences – such as spin–flip energetics or formation enthalpy variations between different magnetic configurations – the systematic component of the dispersion energy is expected to have a very small influence. This expectation is supported by additional single-point calculations performed for the PBE-relaxed ferrimagnetic bulk γ-Fe_2O_3 and magnetic C1–C4 structures using the DFT-D3 (BJ) correction. The differences in formation enthalpies relative to the ferrimagnetic reference state were 60 meV at^{-1} for C1 (compared to 59 meV at^{-1} with PBE), 52 meV at^{-1} for C2 (PBE: 54 meV at$^{-.1}$), 31 meV at^{-1} for C3 (PBE: 30 meV at^{-1}) and 52 meV at^{-1} for C4 (PBE: 54 meV per atom). Moreover, since neither the bulk nor nanoparticle models contain features typically associated with dispersion-dominated systems (e.g., hydrogen bonding, organic ligands, or van der Waals layering), the physical justification for including dispersion corrections is limited. In this context, their role can be interpreted primarily as an empirical adjustment to improve agreement with absolute formation enthalpies, rather than reflecting physically relevant interactions in the system.

Acknowledgements

This journal is © the Owner Societies 2025

Phys. Chem. Chem. Phys., 2025, **27**, 21424–21440 | **21437**

References

1 S. Ahmad, H. Ni, F. S. Al-Mubaddel, M. A. Rizk, M. B. Ammar, A. U. Khan, Z. M. Almarhoon, A. A. Alanazi and M. E. A. Zaki, *Sci. Rep.*, 2025, **15**, 878.

2 Z. L. Lu, W. Q. Zou, L. Y. Lv, X. C. Liu, S. D. Li, J. M. Zhu, F. M. Zhang and Y. W. Du, *J. Phys. Chem. B*, 2006, **110**, 23817.

3 Z.-M. Liao, Y.-D. Li, J. Xu, J.-M. Zhang, K. Xia and D.-P. Yu, *Nano Lett.*, 2006, **6**, 1087.

4 Y. Hadadian, H. Masoomi, A. Dinari, C. Ryu, S. Hwang, S. Kim, B. Cho, J. Y. Lee and J. Yoon, *ACS Omega*, 2022, **7**, 15996.

5 S. J. Kemp, M. R. Ferguson, A. P. Khandhar and K. M. Krishnan, *RSC Adv.*, 2016, **6**, 77452.

6 M. Abbas, M. Takahashi and C. Kim, *J. Nanopart. Res.*, 2013, **15**, 1354.

7 A. Karthick, B. Roy and P. Chattopadhyay, *J. Environ. Manage.*, 2019, **240**, 93.

8 M. Wang, G. Fang, P. Liu, D. Zhou, C. Ma, D. Zhang and J. Zhan, *Appl. Catal., B*, 2016, **188**, 113.

9 M. Li, P. Zhang, M. Adeel, Z. Guo, A. J. Chetwynd, C. Ma, T. Bai, Y. Hao and Y. Rui, *Environ. Pollut.*, 2021, **269**, 116134.

10 Y. Hao, W. Yuan, C. Ma, J. C. White, Z. Zhang, M. Adeel, T. Zhou, Y. Rui and B. Xing, *Environ. Sci.: Nano*, 2018, **5**, 1685.

11 Y. Kong, T. Wu, D. Wu, Y. Zhang, Y. Wang, B. Du and Q. Wei, *Anal. Methods*, 2018, **10**, 4784.

12 M. Babincová, P. Sourivong, D. Leszczynska and P. Babinec, *Med. Hypotheses*, 2000, **55**, 459.

13 U. O. Häfeli, J. S. Riffle, L. Harris-Shekhawat, A. Carmichael-Baranauskas, F. Mark, J. P. Dailey and D. Bardenstein, *Mol. Pharmaceutics*, 2009, **6**, 1417.

14 Q. A. Pankhurst, J. Connolly, S. K. Jones and J. Dobson, *J. Phys. D: Appl. Phys.*, 2003, **36**, 167.

15 F.-H. Chen, L.-M. Zhang, Q.-T. Chen, Y. Zhang and Z.-J. Zhang, *Chem. Commun.*, 2010, **46**, 8633.

16 B. Chertok, A. E. David and V. C. Yang, *Biomaterials*, 2010, **31**, 6317.

17 J. L. Arias, V. Gallardo, M. A. Ruiz and Á. V. Delgado, *Eur. J. Pharm. Biopharm.*, 2008, **69**, 54.

18 R. Weissleder, G. Elizondo, J. Wittenberg, C. A. Rabito, H. H. Bengele and L. Josephson, *Radiology*, 1990, **175**, 489.

19 M. Zhao, D. A. Beauregard, L. Loizou, B. Davletov and K. M. Brindle, *Nat. Med.*, 2001, **7**, 1241.

20 R. Lawaczeck, H. Bauer, T. Frenzel, M. Hasegawa, Y. Ito, K. Kito, N. Miwa, H. Tsutsui, H. Vogler and H. J. Weinmann, *Acta Radiol.*, 1997, **38**, 584.

21 J. Halavaara, P. Tervahartiala, H. Isoniemi and K. Höckerstedt, *Acta Radiol.*, 2002, **43**, 180.

22 R. K. Gilchrist, R. Medal, W. D. Shorey, R. C. Hanselman, J. C. Parrott and C. B. Taylor, *Ann. Surg.*, 1957, **146**, 596.

23 D. C. F. Chan, D. B. Kirpotin and P. A. Bunn Jr., *J. Magn. Magn. Mater.*, 1993, **122**, 374.

24 I. Hilger, K. Frühauf, W. Andrä, R. Hiergeist, R. Hergt and W. A. Kaiser, *Acad. Radiol.*, 2002, **9**, 198.

25 T. Kikumori, T. Kobayashi, M. Sawaki and T. Imai, *Breast Cancer Res. Treat.*, 2009, **113**, 435.

26 F. Gazeau, M. Lévy and C. Wilhelm, *Nanomedicine*, 2008, **3**, 831.

27 S. M. Dadfar, K. Roemhild, N. I. Drude, S. von Stillfried, R. Knüchel, F. Kiessling and T. Lammers, *Adv. Drug Delivery Rev.*, 2019, **138**, 302.

28 C. C. Berry and A. S. G. Curtis, *J. Phys. D: Appl. Phys.*, 2003, **36**, 198.

29 D. Ma, J. Chen, Y. Luo, H. Wang and X. Shi, *J. Mater. Chem. B*, 2017, **5**, 7267.

30 S. R. Ansari, J. Mahajan and A. Teleki, *Wiley Interdiscip. Rev.:Nanomed. Nanobiotechnol.*, 2024, **16**, 1963.

31 J. Yang, J. Feng, S. Yang, Y. Xu and Z. Shen, *Small*, 2023, **19**, 2302856.

32 H. Wei, A. Wiśniowska, J. Fan, P. Harvey, Y. Li, V. Wu, E. C. Hansen, J. Zhang, M. G. Kaul, A. M. Frey, G. Adam, A. I. Frenkel, M. G. Bawendi and A. Jasanoff, *Proc. Natl. Acad. Sci. U. S. A.*, 2021, **118**, 2102340118.

33 A. Lavín Flores, N. Medina-Berríos, W. Pantoja-Romero, D. Berríos Plaza, K. Kisslinger, J. Beltran-Huarac, G. Morell and B. R. Weiner, *ACS Omega*, 2024, **9**, 32980.

34 P. Guardia, R. Di Corato, L. Lartigue, C. Wilhelm, A. Espinosa, M. Garcia-Hernandez, F. Gazeau, L. Manna and T. Pellegrino, *ACS Nano*, 2012, **6**, 3080.

35 A. Espinosa, R. Di Corato, J. Kolosnjaj-Tabi, P. Flaud and T. Pellegrino, *ACS Nano*, 2016, **10**, 2436.

36 Y. Lv, Y. Yang, J. Fang, H. Zhang, E. Peng, X. Liu, W. Xiao and J. Ding, *RSC Adv.*, 2015, **5**, 76764.

37 S. Geng, H. Yang, X. Ren, Y. Liu, S. He, J. Zhou, N. Su, Y. Li, C. Xu, X. Zhang and Z. Cheng, *Chem. – Asian J.*, 2016, **11**, 2996.

38 Z. Zhou, X. Zhu, D. Wu, Q. Chen, D. Huang, C. Sun, J. Xin, K. Ni and J. Gao, *Chem. Mater.*, 2015, **27**, 3505.

39 A. Kirilyuk, A. Fielicke, K. Demyk, G. von Helden, G. Meijer and T. Rasing, *Phys. Rev. B: Condens. Matter Mater. Phys.*, 2010, **82**, 020405(R).

40 A. Erlebach, C. Hühn, R. Jana and M. Sierka, *Phys. Chem. Chem. Phys.*, 2014, **16**, 26421.

41 S. Alaei, S. Jalili and S. Erkoc, *Quantum Matter*, 2016, **5**, 607.

42 X. L. Ding, W. Xue, Y. P. Ma, Z. C. Wang and S. G. He, *J. Chem. Phys.*, 2009, **130**, 014303.

43 G. L. Gutsev, K. G. Belay, K. V. Bozhenko, L. G. Gutsev and B. R. Ramachandran, *Phys. Chem. Chem. Phys.*, 2016, **18**, 27858.

44 G. L. Gutsev, K. G. Belay, L. G. Gutsev and B. R. Ramachandran, *Comput. Mater. Sci.*, 2017, **137**, 134.

21438 | *Phys. Chem. Chem. Phys.*, 2025, **27**, 21424–21440

This journal is © the Owner Societies 2025

45 H. Shiroishi, T. Oda, I. Hamada and N. Fujima, *Eur. Phys. J. D*, 2003, **24**, 85.

46 G. L. Gutsev, K. G. Belay, L. G. Gutsev, B. R. Ramachandran and P. Jena, *Phys. Chem. Chem. Phys.*, 2018, **20**, 4546.

47 R. Khorrampour, H. Raissi, H. Shaki, A. Morsali and H. Hashemzadeh, *Mol. Simul.*, 2020, **46**, 408.

48 H. Lari, A. Morsali and M. M. Heravi, *Z. Phys. Chem.*, 2018, **232**, 579.

49 M. Kamel, H. Raissi, A. Morsali and K. Mohammadifard, *Adsorption*, 2020, **26**, 925.

50 K. Palotás, A. N. Andriotis and A. Lappas, *Phys. Rev. B: Condens. Matter Mater. Phys.*, 2010, **81**, 075403.

51 S. López, A. H. Romero, J. Mejía-López, J. Mazo-Zuluaga and J. Restrepo, *Phys. Rev. B: Condens. Matter Mater. Phys.*, 2009, **80**, 085107.

52 A. Erlebach, H. D. Kurland, J. Grabow, F. A. Müller and M. Sierka, *Nanoscale*, 2015, **7**, 2960.

53 M. Coduri, P. Masala, L. Del Bianco, F. Spizzo, D. Ceresoli, C. Castellano, S. Cappelli, C. Oliva, S. Checchia, M. Allieta, D. V. Szabo, S. Schlabach, M. Hagelstein, C. Ferrero and M. Scavini, *Nanomaterials*, 2020, **10**, 867.

54 S.-H. Yoo, L. Lymerakis and J. Neugebauer, *Phys. Rev. Mater.*, 2021, **5**, 044605.

55 S.-H. Yoo, M. Todorova, D. Wickramaratne, L. Weston, C. G. Van de Walle and J. Neugebauer, *npj Comput. Mater.*, 2021, **7**, 58.

56 X. Huang, E. Lindgren and J. R. Chelikowsky, *Phys. Rev. B: Condens. Matter Mater. Phys.*, 2005, **71**, 165328.

57 H.-X. Deng, S.-S. Li, J. Li and S.-H. Wei, *Phys. Rev. B: Condens. Matter Mater. Phys.*, 2012, **85**, 195328.

58 P. Hohenberg and W. Kohn, *Phys. Rev.*, 1964, **136**, B864.

59 W. Kohn and L. J. Sham, *Phys. Rev.*, 1965, **140**, A1133.

60 G. Kresse and J. Hafner, *Phys. Rev. B: Condens. Matter Mater. Phys.*, 1993, **47**, 558.

61 G. Kresse and J. Hafner, *Phys. Rev. B: Condens. Matter Mater. Phys.*, 1994, **49**, 14251.

62 G. Kresse and J. Furthmüller, *Comput. Mater. Sci.*, 1996, **6**, 15.

63 G. Kresse and J. Furthmüller, *Phys. Rev. B: Condens. Matter Mater. Phys.*, 1996, **54**, 11169.

64 J. P. Perdew, K. Burke and M. Ernzerhof, *Phys. Rev. Lett.*, 1996, **77**, 3865.

65 J. P. Perdew, K. Burke and M. Ernzerhof, *Phys. Rev. Lett.*, 1997, **78**, 1396.

66 P. E. Blöchl, *Phys. Rev. B: Condens. Matter Mater. Phys.*, 1994, **50**, 17953.

67 G. Kresse and D. Joubert, *Phys. Rev. B: Condens. Matter Mater. Phys.*, 1999, **59**, 1758.

68 P. E. Blöchl, O. Jepsen and O. K. Andersen, *Phys. Rev. B: Condens. Matter Mater. Phys.*, 1994, **49**, 16223.

69 M. Methfessel and A. T. Paxton, *Phys. Rev. B: Condens. Matter Mater. Phys.*, 1989, **40**, 3616.

70 C. L. Fu and K. M. Ho, *Phys. Rev. B: Condens. Matter Mater. Phys.*, 1983, **28**, 5480.

71 M. E. Fleet, *Acta Crystallogr., Sect. B: Struct. Sci., Cryst. Eng. Mater.*, 1982, **38**, 1718.

72 J. Guivar, A. Martínez, A. Anaya, L. Valladares, L. Félix and A. Dominguez, *Adv. Nanopart.*, 2014, **3**, 114.

73 P. K. Narnaware and C. Ravikumar, *Inorg. Nano-Met. Chem.*, 2022, **52**, 922.

74 J. Noh, O. I. Osman, S. G. Aziz, P. Winget and J.-L. Brédas, *Sci. Technol. Adv. Mater.*, 2014, **15**, 044202.

75 Y. L. Bentarcurt, M. Calatayud, J. Klapp and F. Ruette, *Surf. Sci.*, 2018, **677**, 239.

76 A. G. Roca, L. Gutiérrez, H. Gavilán, M. E. Fortes Brollo, S. Veintemillas-Verdaguer and M. del Puerto Morales, *Adv. Drug Delivery Rev.*, 2019, **139**, 68.

77 Z. Li, C. Chanéac, G. Berger, S. Delaunay, A. Graff and G. Lefèvre, *RSC Adv.*, 2019, **9**, 33633.

78 Y. Zhang, J. Zhang, K. Tse, L. Wong, C. Chan, B. Deng and J. Zhu, *Sci. Rep.*, 2016, **6**, 20055.

79 M. D. Pashley, *Phys. Rev. B: Condens. Matter Mater. Phys.*, 1989, **40**, 10481.

80 I. P. Suzdalev, Y. B. Maksimov, V. K. Imshennik, S. V. Novichikhin, V. V. Matveev, C.-R. Lin, A. V. Lukashin, P. E. Kazin and Y. D. Treťyakov, *Nanotechnol. Russ.*, 2011, **6**, 743.

81 G. Henkelman, A. Arnaldsson and H. Jónsson, *Comput. Mater. Sci.*, 2006, **36**, 354.

82 M. Yu and D. R. Trinkle, *J. Chem. Phys.*, 2011, **134**, 064111.

83 K. Momma and F. Izumi, *J. Appl. Crystallogr.*, 2011, **44**, 1272.

84 R. M. Cornell and U. Schwertmann, *The Iron Oxides: Structure, Properties, Reactions, Occurrences, and Uses*, Wiley, Weinheim, 2nd edn, 2003.

85 A. Roldan, D. Santos-Carballal and N. H. de Leeuw, *J. Chem. Phys.*, 2013, **138**, 204712.

86 R. Arras, B. Warot-Fonrose and L. Calmels, *J. Phys.: Condens. Matter*, 2013, **25**, 256002.

87 A. N. Shmakov, G. N. Kryukova, S. V. Tsybulya, A. L. Chuvilin and L. P. Solovyeva, *J. Appl. Crystallogr.*, 1995, **28**, 141.

88 A. A. Afify, Z. M. Abd El-Fattah, M. S. M. Esmail and H. H. El-Bahnasawy, *Mater. Today Commun.*, 2023, **35**, 106193.

89 A. Sahu, J. Parize and C. Dupont, *Appl. Surf. Sci.*, 2023, **630**, 157467.

90 H.-T. Jeng and G. Y. Guo, *Phys. Rev. B: Condens. Matter Mater. Phys.*, 2002, **65**, 094429.

91 R. Grau-Crespo, A. Y. Al-Baitai, I. Saadoune and N. H. De Leeuw, *J. Phys.: Condens. Matter*, 2010, **22**, 255401.

92 G. Righi and R. Magri, *J. Phys. Chem. C*, 2019, **123**, 15648.

93 V. C. Rakhecha and N. S. S. Murthy, *J. Phys. C: Solid State Phys.*, 1978, **11**, 4389.

94 C. A. Greaves, *J. Solid State Chem.*, 1983, **49**, 325.

95 R. Dronskowski, *Adv. Funct. Mater.*, 2001, **11**, 27.

96 G. S. Parkinson, *Surf. Sci. Rep.*, 2016, **71**, 272.

97 T. Hiemstra, *Environ. Sci.: Nano*, 2018, **5**, 752.

98 E. Bianchetti and C. Di Valentin, *J. Phys. Chem. Lett.*, 2022, **13**, 9348.

99 S. Eddahri, A. Razouk, M. Karimou, M. Sajieddine and M. Sahlaoui, *Appl. Phys. A: Mater. Sci. Process.*, 2019, **125**, 694.

This journal is © the Owner Societies 2025

Phys. Chem. Chem. Phys., 2025, **27**, 21424–21440 | **21439**

100 N. Pizúrová, J. Buršík, T. Sojková, P. Roupcová and O. Schneeweiss, *J. Phys.: Conf. Ser.*, 2022, **2315**, 012023.

101 S. Linderoth, P. V. Hendriksen, F. Bødker, S. Wells, K. Davies, S. W. Charles and S. Mørup, *J. Appl. Phys.*, 1994, **75**, 6583.

102 B. H. Kim, N. Lee, H. Kim, K. An, Y. I. Park, Y. Choi, K. Shin, Y. Lee, S. G. Kwon, H. B. Na, J.-G. Park, T.-Y. Ahn, Y.-W. Kim, W. K. Moon, S. H. Choi and T. Hyeon, *J. Am. Chem. Soc.*, 2011, **133**, 12624.

103 S. Grimme, J. Antony, S. Ehrlich and H. Krieg, *J. Chem. Phys.*, 2010, **132**, 154104.

104 S. Grimme, S. Ehrlich and L. Goerigk, *J. Comput. Chem.*, 2011, **32**, 1456.